Monthly Notices of the ROYAL ASTRONOMICAL SOCIETY

MNRAS **524,** 1893–1908 (2023)
Advance Access publication 2023 June 22

https://doi.org/10.1093/mnras/stad1744

A new buoyancy instability in galaxy clusters due to streaming cosmic rays

Philipp Kempski,[1]★ Eliot Quataert [2] and Jonathan Squire [3]

[1]*Department of Astronomy and Theoretical Astrophysics Center, University of California, University Dr, Berkeley, CA 94720, USA*
[2]*Department of Astrophysical Sciences, Princeton University, 4 Ivy Ln, Princeton, NJ 08544, USA*
[3]*Department of Physics, University of Otago, 730 Cumberland St, North Dunedin, Dunedin 9016, New Zealand*

Accepted 2023 May 30. Received 2023 March 24; in original form 2022 July 20

ABSTRACT

Active Galactic Nuclei (AGN) are believed to provide the energy that prevents runaway cooling of gas in the cores of galaxy clusters. However, how this energy is transported and thermalized throughout the Intracluster Medium (ICM) remains unclear. In recent work, we showed that streaming cosmic rays (CRs) destabilize sound waves in dilute ICM plasmas. Here, we show that CR streaming in the presence of gravity also destabilizes a pressure-balanced wave. We term this new instability the CR buoyancy instability (CRBI). In stark contrast to standard results without CRs, the pressure-balanced mode is highly compressible at short wavelengths due to CR streaming. Maximal growth rates are of order $(p_c/p_g)\beta^{1/2}\omega_{\rm ff}$, where p_c/p_g is the ratio of CR pressure to thermal gas pressure, β is the ratio of thermal to magnetic pressure, and $\omega_{\rm ff}$ is the free-fall frequency. The CRBI operates alongside buoyancy instabilities driven by background heat fluxes, i.e. the heat-flux-driven buoyancy instability (HBI) and the magneto-thermal instability (MTI). When the thermal mean free path $l_{\rm mfp}$ is $\ll$ the gas scale height H, the HBI/MTI set the growth rate on large scales, while the CRBI sets the growth rate on small scales. Conversely, when $l_{\rm mfp} \sim H$ and $(p_c/p_g)\beta^{1/2} \gtrsim 1$, CRBI growth rates exceed HBI/MTI growth rates even on large scales. Our results suggest that CR-driven instabilities may be partially responsible for the sound waves/weak shocks and turbulence observed in galaxy clusters. CR-driven instabilities generated near radio bubbles may also play an important role redistributing AGN energy throughout clusters.

Key words: instabilities – plasmas – cosmic rays – galaxies: clusters: intracluster medium – galaxies: evolution.

1 INTRODUCTION

The cores of galaxy clusters are filled with virialized, hot gas, with typical temperatures exceeding 10^7 K. The X-ray luminosities of most cluster cores imply cooling times that are significantly shorter than the ages of these systems. Without a source of heating, this hot gas is expected to cool, sink to the center and form stars at a high rate. However, observations find significantly smaller star formation rates and cold gas masses than are predicted by the 'cooling flow' model (e.g. Peterson & Fabian 2006). This suggests that there is a source of heating present that keeps the gas in cluster cores in approximate thermal balance.

Central Active Galactic Nuclei (AGN) and the interaction of their jets with the Intracluster Medium (ICM) are believed to play an important role in providing the energy that prevents runaway cooling of ICM gas. In particular, observations suggest that energy is carried away from the central AGN by jet-inflated bubbles of relativistic plasma that buoyantly rise into the ICM. There is a strong correlation between the power needed to inflate the bubbles and the radiative losses of the hot gas (Churazov et al. 2000; Bîrzan et al. 2004; Rafferty et al. 2006; Nulsen et al. 2009; Hlavacek-Larrondo et al. 2012; see Werner et al. 2019 for a recent review).

How this energy is subsequently transported and thermalized throughout cluster cores remains an open question. It is possible that the buoyantly rising radio bubbles stir turbulence by exciting internal gravity waves (IGWs; e.g. Zhuravleva et al. 2016; Zhang, Churazov & Schekochihin 2018), launch sound waves and/or weak shocks (e.g. Fabian et al. 2003, 2006; Sternberg & Soker 2009), and/or inject cosmic rays (CRs) into the ICM (e.g. Guo & Oh 2008; Jacob & Pfrommer 2017a; Jacob & Pfrommer 2017b). These processes can plausibly occur to some extent simultaneously, but it is unclear which (if any) one is the dominant channel for ICM heating.

Relativistic CRs from both star formation and AGN may play an important role in the evolution of gas in clusters by driving outflows and heating diffuse gas (e.g. Breitschwerdt, McKenzie & Voelk 1991; Loewenstein, Zweibel & Begelman 1991; Everett et al. 2008; Socrates, Davis & Ramirez-Ruiz 2008; Guo & Oh 2008; Zweibel 2013, 2017; Ruszkowski, Yang & Zweibel 2017; Jacob & Pfrommer 2017a, b; Ehlert et al. 2018; Farber et al. 2018; Kempski & Quataert 2020; Quataert, Jiang & Thompson 2022a; Quataert, Thompson & Jiang 2022b). CRs couple to the thermal gas by scattering from small-scale magnetic fluctuations. In self-confinement theory, CRs are scattered by Alfvén waves propagating down the CR pressure gradient, which they themselves excite through the streaming instability (Kulsrud & Pearce 1969). Pitch-angle scattering by the excited Alfvén waves isotropises the CRs in the frame of the waves. In the absence of damping of the self-excited waves, this results in CR streaming relative to the thermal gas at the local Alfvén speed. If damping is present, CR propagation deviates from pure Alfvénic streaming. The form of the transport correction is, however, quite peculiar, as it corresponds to neither streaming nor diffusion

★ E-mail: pkempski@princeton.edu

(Skilling 1971, Wiener, Oh & Guo 2013; Kempski & Quataert 2022).

In recent work, we showed that streaming CRs drive a rapidly growing acoustic instability in dilute ICM plasmas, the Cosmic Ray Acoustic Braginskii (CRAB) instability (Kempski, Quataert & Squire 2020). This suggests that the different channels for transferring and thermalizing energy in the ICM (waves, CRs, turbulence...), usually considered separately in theoretical models, may in fact be closely related. Here, we demonstrate that in the presence of gravity, streaming CRs also destabilize a pressure-balanced wave, more specifically the CR entropy mode modified by gravity. We term this instability the CR buoyancy instability (CRBI) because CRs and buoyancy (gravity) are critical for setting its properties. The growth rates of the CRBI are of order the natural buoyancy frequency (the local free-fall frequency) for plausible ICM parameters. Our work demonstrates the potential physical richness of CR feedback in dilute plasmas: both the CRBI considered in this work and the CRAB instability in Kempski et al. (2020) are driven by CR streaming at the Alfvén speed, which in a weakly collisional plasma depends on the pressure anisotropy of the thermal gas (the pressure is anisotropic because of the large thermal-particle mean free path in the ICM). This dependence introduces a new form of coupling between the CRs and the thermal gas, which is very unstable.

The remainder of this work is organized as follows. We present our model of CRs coupled to a low-collisionality plasma in Section 2. In Section 3, we provide a physical overview of the instability. We derive a dispersion relation and asymptotic growth rates in Section 4. In Section 5, we present numerical solutions to the linearized system of equations for an isothermal background. We discuss the relationship to other buoyancy instabilities and thermal instability, and the importance of CR diffusion in Section 6. We summarize our results in Section 7.

2 MODEL

2.1 Equations

We consider a low-collisionality plasma coupled to streaming CRs. We use the weakly collisional Braginskii MHD model to describe the thermal gas (Braginskii 1965). The equations for the gas and CRs are,

$$\frac{\partial \rho}{\partial t} + \nabla\cdot(\rho \mathbf{v}) = 0, \tag{1}$$

$$\rho \frac{d\mathbf{v}}{dt} = -\nabla\left(p_\perp + p_c + \frac{B^2}{8\pi}\right) + \frac{\boldsymbol{B}\cdot\nabla\boldsymbol{B}}{4\pi} + \nabla\cdot(\hat{\boldsymbol{b}}\hat{\boldsymbol{b}}\Delta p) + \rho \boldsymbol{g}, \tag{2}$$

$$\frac{\partial \boldsymbol{B}}{\partial t} = \nabla\times(\mathbf{v}\times\boldsymbol{B}), \tag{3}$$

$$\rho T \frac{ds}{dt} = -\mathbf{v}_{\mathbf{st},\Delta p}\cdot\nabla p_c - \boldsymbol{\Pi} : \nabla\mathbf{v} - \nabla\cdot\boldsymbol{Q} - \rho^2\Lambda(T), \tag{4}$$

$$\frac{dp_c}{dt} = -\frac{4}{3}p_c\nabla\cdot(\mathbf{v}+\mathbf{v}_{\mathbf{st},\Delta p}) - \mathbf{v}_{\mathbf{st},\Delta p}\cdot\nabla p_c + \nabla\cdot(\kappa\hat{\boldsymbol{b}}\hat{\boldsymbol{b}}\cdot\nabla p_c), \tag{5}$$

where $\mathbf{v}$ is the gas velocity, ρ is the gas density, $\boldsymbol{B}$ is the magnetic field (with unit vector $\hat{\boldsymbol{b}}$), $s = k_\mathrm{B}\ln(p_g/\rho^\gamma)/(\gamma-1)m_\mathrm{H}$ is the gas entropy per unit mass, $\Lambda(T)$ is the temperature-dependent cooling function, and p_c is the CR pressure. $d/dt \equiv \partial/\partial t + \mathbf{v}\cdot\nabla$ denotes a total (Lagrangian) time derivative. $\Delta p = p_\perp - p_\parallel$ is the gas pressure anisotropy, where $p_\perp$ and $p_\parallel$ denote the pressures in the directions perpendicular and parallel to the magnetic field, respectively. $p_\perp$ and $p_\parallel$ are related to p_g in equation (4) by

$$p_\perp = p_g + \frac{1}{3}\Delta p. \tag{6}$$

The pressure anisotropy in Braginskii MHD (with viscosity $\nu_\mathrm{B} \approx p_g/\rho\nu_\mathrm{ii}$, where ν_ii is the ion–ion collision rate; Braginskii 1965) is given by

$$\Delta p = p_\perp - p_\parallel = 3\rho\nu_\mathrm{B}\left(\hat{\boldsymbol{b}}\hat{\boldsymbol{b}} : \nabla\mathbf{v} - \frac{1}{3}\nabla\cdot\mathbf{v}\right). \tag{7}$$

The viscous stress tensor in the gas-entropy equation is

$$\boldsymbol{\Pi} = -\Delta p\left(\hat{\boldsymbol{b}}\hat{\boldsymbol{b}} - \frac{\boldsymbol{\mathcal{I}}}{\mathbf{3}}\right). \tag{8}$$

In the absence of background Δp, the perturbed $\boldsymbol{\Pi} : \nabla\mathbf{v}$ in the gas-entropy equation is second-order and does not contribute in our linear analysis. $\boldsymbol{Q}$ in equation (4) is the anisotropic thermal heat flux,

$$\boldsymbol{Q} = -\kappa_\mathrm{B}\hat{\boldsymbol{b}}\hat{\boldsymbol{b}}\cdot\nabla T, \tag{9}$$

where κ_B is the thermal conductivity.

$\mathrm{v}_{\mathrm{st},\Delta p}$ in equation (5) is the CR streaming speed. We assume that CRs stream down their pressure gradient at the Alfvén speed, which in low-collisionality plasmas depends on the thermal-gas pressure anisotropy,[1]

$$\mathbf{v}_{\mathbf{st},\Delta p} = \chi\mathbf{v}_{\mathbf{A},\Delta p} = \chi\mathrm{v}_\mathrm{A}\left(1 + \frac{4\pi\Delta p}{B^2}\right)^{1/2}, \tag{10}$$

where $\mathrm{v}_\mathrm{A} = \boldsymbol{B}/\sqrt{4\pi\rho}$ is the Alfvén velocity in the absence of pressure anisotropy, and $\chi \equiv -\hat{\boldsymbol{b}}\cdot\nabla p_c/|\hat{\boldsymbol{b}}\cdot\nabla p_c| = \pm 1$ ensures that the CRs stream along $\boldsymbol{B}$ down their pressure gradient and makes the CR heating term $-\mathbf{v}_{\mathbf{st},\Delta p}\cdot\nabla p_c$ in the gas energy equation (4) positive definite. We also include CR diffusion along the magnetic field in equation (5).

2.2 Dimensionless parameters and characteristic frequencies

We define the ratio of CR pressure to gas pressure,

$$\eta \equiv \frac{p_c}{p_g}, \tag{11}$$

and the ratio of thermal to magnetic pressure,

$$\beta \equiv \frac{8\pi p_g}{B^2}. \tag{12}$$

The relevant frequencies are the gas sound frequency (with c_s being the isothermal gas sound speed),

$$\omega_s \equiv k c_s; \tag{13}$$

the Alfvén *and* CR-streaming frequency,

$$\omega_\mathrm{A} \equiv \boldsymbol{k}\cdot\mathbf{v}_\mathbf{A}; \tag{14}$$

the CR diffusion frequency,

$$\omega_d \equiv \kappa\,(\hat{\boldsymbol{b}}\cdot\boldsymbol{k})^2; \tag{15}$$

the free-fall frequency,

$$\omega_\mathrm{ff} \equiv \frac{g}{c_s} = \frac{c_s}{H}, \tag{16}$$

[1]We note that the original expression for the Alfvén speed in Kempski et al. (2020) was incorrect, as the 1/2 exponent in the Δp term in equation (10) was by accident omitted. This was corrected in Kempski, Quataert & Squire (2021). However, the conclusions of Kempski et al. (2020) are not affected by this change.

where H is the gas scale height; the cooling frequency,

$$\omega_c \equiv \frac{\rho^2 \Lambda}{p_g}; \tag{17}$$

the ion–ion collision frequency $\nu_{\rm ii}$ and the associated Braginskii viscous frequency,

$$\omega_{\rm B} \equiv \nu_{\rm B}(\hat{\boldsymbol{b}}\cdot\boldsymbol{k})^2 \approx \frac{p_g}{\rho\nu_{\rm ii}}(\hat{\boldsymbol{b}}\cdot\boldsymbol{k})^2; \tag{18}$$

and the conductive frequency,

$$\omega_{\rm cond} \equiv \chi_{\rm B}(\hat{\boldsymbol{b}}\cdot\boldsymbol{k})^2, \tag{19}$$

where $\chi_{\rm B} = \kappa_{\rm B}/nk_{\rm B}$ is the thermal diffusion coefficient. We can relate the diffusive time-scales by defining the thermal Prandtl number,

$${\rm Pr} \equiv \frac{\nu_{\rm B}}{\chi_{\rm B}}. \tag{20}$$

We use ${\rm Pr} = 0.02$ as the default thermal Prandtl number in this work ($\approx$ square root of the electron-to-ion mass ratio), i.e. heat conduction due to electrons operates on a much shorter time-scale than viscous forces due to the ions. We also define the ratio of the CR diffusion coefficient to the Braginskii viscosity,

$$\Phi \equiv \frac{\kappa}{\nu_{\rm B}}, \tag{21}$$

which turns out to be an important parameter quantifying the suppression of the CRBI and CRAB instability by CR diffusion (see also Kempski et al. 2020).

2.3 Validity of the model

2.3.1 Thermal gas

The CR entropy mode describes the response of the two-fluid CR–thermal gas system to a CR pressure perturbation. Since CRs propagate along field lines at the Alfvén speed, this mode is characterized by a frequency of order $\omega_{\rm A}$ (absent CR diffusion). The collisional (Braginskii MHD) regime then requires that $\omega_{\rm A} \ll \nu_{\rm ii}$, or equivalently $kl_{\rm mfp} \ll \beta^{1/2}$. In addition, the assumption that the heat fluxes are due to electrons (${\rm Pr} \approx 0.02$) is valid if the electron-ion thermal equilibration rate is $\gg\omega_{\rm A}$. The electron–ion thermal equilibration rate is slower than the ion–ion collision rate by the square root of the electron-to-ion mass ratio, $\tau_{\rm eq}^{-1} \sim (m_e/m_i)^{1/2}\nu_{\rm ii} \sim \nu_{\rm ii}/40$, which means that ions and electrons are thermally coupled for $\omega \sim \omega_{\rm A}$ modes if $kl_{\rm mfp} \ll \beta^{1/2}/40$. We will typically assume $\beta \sim 100$ and so the Braginskii MHD model employed here is valid for $kl_{\rm mfp} \ll 1$. Throughout the paper we show results of our calculations for $kl_{\rm mfp} \lesssim 1$ although we stress that the Braginskii model is not strictly valid for $kl_{\rm mfp} \sim 1$. However, our results using collisionless fluid models (Section 6.3 and Fig. 10) suggest that the growth rates are qualitatively similar for $kl_{\rm mfp} > 1$.

We further note that the expression for the pressure anisotropy in (7) ignores the effect of heat fluxes on Δp (Mikhailovskii & Tsypin 1971). In particular, in the collisional limit the pressure anisotropy in the presence of heat fluxes is (e.g. Schekochihin et al. 2010),

$$\Delta p = 3\rho\nu_{\rm B}\left(\hat{\boldsymbol{b}}\hat{\boldsymbol{b}} : \boldsymbol{\nabla}\mathbf{v} - \frac{1}{3}\boldsymbol{\nabla}\cdot\mathbf{v} - \frac{\boldsymbol{\nabla}\cdot[(q_\perp - q_\parallel)\hat{\boldsymbol{b}}] + 3q_\perp\boldsymbol{\nabla}\cdot\hat{\boldsymbol{b}}}{3p_\parallel}\right), \tag{22}$$

where $q_\perp$ and $q_\parallel$ are the parallel fluxes of perpendicular and parallel heat, respectively. In the high-collisionality limit with $\Delta p \ll p_g$, the heat fluxes are $q_\perp \approx q_\parallel/3 \approx -\kappa_{\rm B}\hat{\mathbf{b}}\cdot\nabla T$ where $\kappa_{\rm B}$ is the thermal conductivity, $T = p_g/nk_{\rm B}$ and p_g is given by (6). In this limit, we find that the results of this paper are not significantly affected by the heat-flux term in equation (22). We thus use equation (7) for simplicity throughout this work. However, we note that the collisional expressions for Δp, $q_\perp$ and $q_\parallel$ are not valid on scales approaching the ion mean free path. In this limit, separate evolution equations for the ion and electron perpendicular and parallel pressures should be considered. We briefly discuss this regime in Section 6.3 and Appendix A, focusing on the ions. Our results suggest that the CRBI is qualitatively similar in the low-collisionality limit (Fig. 10).

In the dilute and hot ICM, the ion-ion collision rate is small

$$\nu_{\rm ii} \sim \frac{n_{\rm i}e^4\pi\ln\Lambda}{m_{\rm i}^{1/2}(k_{\rm B}T)^{3/2}} \sim 8\times10^{-14}{\rm s}^{-1}\left(\frac{T}{5\times10^7\ {\rm K}}\right)^{-3/2}\frac{n_{\rm i}}{0.01\ {\rm cm}^{-3}}, \tag{23}$$

for a Coulomb logarithm $\ln\Lambda \approx 38$. The collision rate in (23) corresponds to a mean free path of order 0.1 kpc.

2.3.2 CRs

The CR pressure equation (equation (5)) is a good model for the CRs if the collision frequency of the energetically important GeV CRs is much larger than any other time-scale of interest. As pointed out in Kempski et al. (2020), the GeV CR collision frequency (the rate at which the pitch angle changes by order unity, due to scattering by magnetic fluctuations) is likely much higher than the thermal ion-ion collision frequency in the ICM:

$$\nu_{\rm CR} \sim \Omega_0\left(\frac{\delta B_\perp}{B}\right)^2 \sim 10^{-8}\ {\rm s}^{-1}\left(\frac{\delta B_\perp/B}{10^{-3}}\right)^2, \tag{24}$$

where Ω_0 is the non-relativistic gyro-frequency and $\delta B_\perp/B$ is evaluated for fluctuations whose wavelength parallel to the mean B-field is of order the Larmor radius of the GeV particles. The above collision frequency corresponds to a CR mean free path of order 1 pc, which approximately corresponds to the empirically derived CR mean free path in the Milky Way (e.g. Amato & Blasi 2018). This suggests that treating CRs as collisional on thermal-ion-mean-free-path scales is a reasonable model for the ICM.

In the limit of good coupling between the GeV CRs and the self-excited Alfvén waves (large pitch-angle scattering rate), CR transport is to leading order described by Alfvénic streaming. Damping of the self-excited Alfvén waves introduces corrections to Alfvénic streaming. We model this by also including CR diffusion in our linear analysis. As we will show, significant CR diffusion suppresses the CRBI on small scales.

2.4 Background equilibrium

We consider static background equilibria with constant $\boldsymbol{B} = (B_x, 0, B_z)$, in which the CR and gas pressure gradients balance gravity, $\boldsymbol{g} = -g\hat{\boldsymbol{z}}$,

$$\frac{d}{dz}(p_g + p_c) = -\rho g. \tag{25}$$

If CR diffusion does not affect the background state (either because $\kappa = 0$ or $dp_c/dz = {\rm const}$), CRs are in equilibrium according to equation (5) if $p_c \propto {\rm v_A}^{-4/3}$, or equivalently,

$$p_c \propto \rho^{2/3}. \tag{26}$$

In this work we perturb equilibria that satisfy equations (25) and (26), although these equations do not yet constrain the background

temperature $T(z)$. We will consider different temperature profiles in Sections 5 and 6.

2.5 Linearized equations

We carry out a linear stability calculation of the CR–thermal gas equations (Section 2.1) for backgrounds that satisfy equations (25) and (26). We focus on short-wavelength modes satisfying $kH \gg 1$ (in Fig. 8 we include $kH \sim 1$ modes just to show growth rates of previously identified buoyancy instabilities) and perform a local WKB calculation in which all perturbed quantities are assumed to vary as $\delta X(\boldsymbol{r}, t) \propto \exp(i\boldsymbol{k}\cdot\boldsymbol{r} - i\omega t)$. We consider two coordinate systems in this work. We will mostly use the usual Cartesian coordinate system with the z-axis antiparallel to $\boldsymbol{g}$ and x and y defining the plane perpendicular to gravity. We define associated polar angles such that $B_x = B\sin\theta_B, B_z = B\cos\theta_B, k_x = k\sin\theta_k\cos\phi_k$, $k_y = k\sin\theta_k\sin\phi_k$, and $k_z = k\cos\theta_k$. We use $\phi_k = 0$ in all the figures except Fig. 6, because $\phi_k = 0$ captures the fastest-growing mode. For analytic purposes, it is convenient to also use a coordinate system aligned with the direction of the magnetic field. We define $\perp$ and $\parallel$ to denote the directions perpendicular and parallel to the magnetic field. We will use this coordinate system in Section 4 when we derive an approximate dispersion relation, as it makes the analytics more tractable. However, when we plot numerically calculated growth rates of the instability in Figs 2–10, we adopt the more standard notation with directions/angles defined relative to the positive z-direction, i.e. $\cos\theta_B \equiv -\hat{\boldsymbol{b}}\cdot\hat{\boldsymbol{g}}$ and $\cos\theta_k \equiv -\hat{\boldsymbol{k}}\cdot\hat{\boldsymbol{g}}$.

The linearized equations are

$$\omega\frac{\delta\rho}{\rho} = \boldsymbol{k}\cdot\mathbf{v} - i\mathrm{v}_z\frac{d\ln\rho}{dz}\times\mathrm{BG}, \tag{27}$$

$$\omega\mathbf{v} = \boldsymbol{k}c_s^2\left(\frac{\delta p_\perp}{p_g} + \eta\frac{\delta p_c}{p_c} + \frac{\mathrm{v_A}^2}{c_s^2}\frac{\delta B_\parallel}{B}\right) - \omega_\mathrm{A}\mathrm{v_A}\frac{\boldsymbol{\delta B}}{B} - \hat{\boldsymbol{b}}(\hat{\boldsymbol{b}}\cdot\boldsymbol{k})c_s^2\frac{\delta\Delta p}{p_g} + i\boldsymbol{g}\frac{\delta\rho}{\rho}, \tag{28}$$

$$\omega\frac{\boldsymbol{\delta B}_\perp}{B} = -k_\parallel\mathbf{v}_\perp, \tag{29}$$

$$\omega\frac{\delta B_\parallel}{B} = \boldsymbol{k}_\perp\cdot\mathbf{v}_\perp, \tag{30}$$

$$\omega\frac{\delta p_g}{p_g} = \gamma\boldsymbol{k}\cdot\mathbf{v} - i(\gamma-1)\omega_\mathrm{cond}\left(\frac{\delta p_g}{p_g} - \frac{\delta\rho}{\rho}\right) + \chi\eta(\gamma-1)\omega_\mathrm{A}\frac{\delta p_c}{p_c} - i(\gamma-1)\omega_c\frac{\partial\ln\Lambda}{\partial\ln T}\frac{\delta p_g}{p_g} - i(\gamma-1)\omega_c\left(2 - \frac{\partial\ln\Lambda}{\partial\ln T}\right)\frac{\delta\rho}{\rho} + \mathrm{BG}\times\left[-i\mathrm{v}_z\frac{d\ln p_g}{dz} - i\chi\eta(\gamma-1)\delta\mathrm{v}_{\mathrm{A},z}\frac{d\ln p_c}{dz} + \frac{i(\gamma-1)}{T}\nabla\cdot(\chi_\mathrm{B}\boldsymbol{\delta}\hat{\mathbf{b}}\hat{\mathbf{b}}\cdot\nabla T + \chi_\mathrm{B}\hat{\mathbf{b}}\boldsymbol{\delta}\hat{\mathbf{b}}\cdot\nabla T)\right], \tag{31}$$

$$\frac{\delta\Delta p}{p_g} = i\frac{\rho\nu_\mathrm{B}}{p_g}(2k_\parallel\mathrm{v}_\parallel - \boldsymbol{k}_\perp\cdot\mathbf{v}_\perp). \tag{32}$$

$$\omega\frac{\delta p_c}{p_c} = \frac{4}{3}\boldsymbol{k}\cdot\mathbf{v} - \frac{2}{3}\chi\omega_\mathrm{A}\frac{\delta\rho}{\rho} + \frac{1}{3}\beta\chi\omega_\mathrm{A}\frac{\delta\Delta p}{p_g} + (\chi\omega_\mathrm{A} - i\omega_d)\frac{\delta p_c}{p_c} + \mathrm{BG}\times\left[-i\mathrm{v}_z\frac{d\ln p_c}{dz} + \frac{2}{3}i\chi\mathrm{v}_{\mathrm{A},z}\frac{d\ln\rho}{dz}\left(\frac{\delta p_c}{p_c} - \frac{\delta\rho}{\rho}\right) + \frac{i}{p_c}\nabla\cdot(\kappa\boldsymbol{\delta}\hat{\mathbf{b}}\hat{\mathbf{b}}\cdot\nabla p_c + \kappa\hat{\mathbf{b}}\boldsymbol{\delta}\hat{\mathbf{b}}\cdot\nabla p_c)\right], \tag{33}$$

where BG in equations (27)–(33) is a flag equal to 1 or 0. It specifies whether gradients from the background equilibrium in equations (25) and (26), i.e. terms of the form $\mathrm{v}_z d\rho/dz$, are included in the calculation. Without the background gradients equilibrium is not satisfied and so the BG terms should formally be kept in the linear perturbation analysis. However, for analytic simplicity, we set BG = 0 when we discuss the physics of the instability and derive approximate dispersion relations in Sections 3.2, 3.3, and 4. This turns out to be a reasonable approximation, as the CRBI is not directly driven by the background gradients. We do, however, include background gradients, i.e. we set BG = 1, when we solve for the exact eigenmodes numerically (Section 5 and all the figures presented in this paper).

3 PHYSICAL OVERVIEW OF THE INSTABILITY

In this section, we provide an overview of the key physics describing the CRBI. To start, we give a brief summary of entropy and gravity waves in stratified CR MHD (Section 3.1). This will set the stage for our analysis and elucidate how the CRBI is related to other instabilities that may operate in the ICM (such as thermal instability or other buoyancy instabilities).

3.1 Gravity and entropy modes in stratified media

3.1.1 MHD modes

In a gravitationally stratified medium without magnetic fields, the hydrodynamic entropy mode becomes an IGW characterized by the Brunt–Väisälä frequency (e.g. Defouw 1970),

$$N^2 = \frac{g}{\gamma}\left(\frac{d\ln p_g}{dz} - \gamma\frac{d\ln\rho}{dz}\right). \tag{34}$$

In MHD, gravitational stratification affects the MHD slow magnetosonic modes, as both buoyancy and magnetic tension act as the modes' restoring forces (e.g. Defouw 1970, Stein & Leibacher 1974). The resulting mode resembles the hydro IGW at long wavelengths, and the standard MHD slow mode (absent gravity) at short wavelengths. In contrast to hydrodynamics, in MHD there is also a mode that is unaffected by buoyancy despite a non-zero density perturbation (Defouw 1970). We refer to this mode as the MHD entropy mode.

We now compute these modes more explicitly in high-β collisional MHD, first assuming that no CRs are present. For simplicity, we shall consider the 2D case with $\boldsymbol{B} = B\hat{\boldsymbol{z}}$, $\boldsymbol{g} = -g\hat{\boldsymbol{z}}$, and $\boldsymbol{k}$ in the x–z plane. We start with the momentum equation,

$$\omega\mathbf{v} = \boldsymbol{k}c_s^2\left(\frac{\delta p_g}{p_g} + \frac{\mathrm{v_A}^2}{c_s^2}\frac{\delta B}{B}\right) - \omega_\mathrm{A}\mathrm{v_A}\frac{\boldsymbol{\delta B}}{B} - i\frac{\delta\rho}{\rho}g\hat{\boldsymbol{z}}. \tag{35}$$

Crossing the momentum equation twice with $\boldsymbol{k}$ and taking the z-component we find,

$$\omega^2(k_z k_x\mathrm{v}_x - k_x^2\mathrm{v}_z) = \omega_\mathrm{A}\mathrm{v_A}k^2k_x\mathrm{v}_x + i\omega g k_x^2\frac{\delta\rho}{\rho}. \tag{36}$$

In the Boussinesq limit ($\delta p_g/p_g \ll \delta\rho/\rho$), the adiabatic gas entropy equation $ds/dt = 0$ (equation (31) without CRs, cooling and conduction) implies that

$$\omega\frac{\delta\rho}{\rho} = \frac{i}{\gamma}\mathrm{v}_z\left(\frac{d\ln p_g}{dz} - \gamma\frac{d\ln\rho}{dz}\right) = i\frac{\mathrm{v}_z}{g}N^2. \tag{37}$$

Using incompressibility $k_x\mathrm{v}_x \approx -k_z\mathrm{v}_z$ we find the dispersion relation for MHD slow modes modified by gravity,

$$\omega^2k^2 = \omega_\mathrm{A}\mathrm{v_A}k^2k_z + k_x^2\frac{g}{\gamma}\left(\frac{d\ln p_g}{dz} - \gamma\frac{d\ln\rho}{dz}\right), \tag{38}$$

or,

$$\omega^2 = \omega_{\rm A}^2 + \frac{k_x^2}{k^2} N^2. \quad (39)$$

For subdominant magnetic tension (first term on RHS) we get the usual dispersion relation for the two hydrodynamic IGWs, $\omega = \pm N k_x/k$. At short wavelengths where magnetic tension dominates, the two gravity waves satisfy the standard dispersion relation for the MHD slow modes at high β.

Unlike the hydrodynamic entropy mode, the MHD entropy mode does not pick up a buoyancy response. To see why this is the case, we first note that a mode with $\omega = 0$ and $\mathbf{v} = 0$, but finite $\delta\rho/\rho$, satisfies the continuity (equation (27)), induction (equations (29) and (30)), as well as the gas-entropy (equation (31) absent heating, cooling, and conduction) equations. In hydrodynamics, however, this mode does not satisfy the momentum equation (see equation (35) without the perturbed magnetic field), as the direction of gravity and $\boldsymbol{k}$ are generally not co-linear. By contrast, in MHD the perturbed pressure and magnetic-tension terms (first and second terms on the RHS of equation (35)) are mutually orthogonal and can exactly cancel the perturbed gravitational force. As a result, while a mode with $\omega = 0$ and $\mathbf{v} = 0$, but finite $\delta\rho/\rho$, is not an eigenmode in stratified hydrodynamics, it is an eigenmode in stratified MHD and involves a finite $\boldsymbol{\delta B}$ perturbation. When magnetic tension is negligible, i.e. in the hydrodynamic limit with $\omega_{\rm A} \ll N$ (long wavelengths or $\beta \to \infty$), the $\omega = 0$ mode can only be satisfied if $\delta B/B \gg \delta\rho/\rho$. The hydrodynamic variables are therefore essentially unperturbed in this limit, which is consistent with the result in stratified hydrodynamics.

3.1.2 CR MHD modes

When Alfvénically streaming CRs are present, the CR pressure equation (equation (5)) introduces a new mode, which we refer to as the CR entropy mode. Because CRs are assumed to stream at the Alfvén speed along field lines, the CR entropy mode is characterized by the Alfvén frequency, $\omega = \chi \boldsymbol{k} \cdot \mathbf{v_A} = \chi \omega_{\rm A}$ (although the eigenfrequency can deviate appreciably from the Alfvén frequency if CR diffusion is important or if $\eta \gtrsim 1$ due to the fact that the CR entropy mode is then associated with significant density fluctuations). The χ factor in front of $\omega_{\rm A}$ reflects the fact that the CR entropy mode propagates down the CR pressure gradient. For $\eta \to 0$ the impact of CRs on the thermal gas is small, and so the CR entropy mode does not perturb the thermal gas. Using that the background density gradient satisfies $2d\ln\rho/dz = 3d\ln p_c/dz$ in equilibrium, (33) becomes,

$$\left(\omega - \chi\omega_{\rm A} + i\omega_d - i\chi {\rm v}_{{\rm A},z} \frac{d\ln p_c}{dz}\right) \frac{\delta p_c}{p_c} \approx 0, \quad (40)$$

with solution,

$$\omega = \chi\omega_{\rm A} - i\omega_d + i\chi {\rm v}_{{\rm A},z} \frac{d\ln p_c}{dz}. \quad (41)$$

Diffusive corrections to CR streaming act to damp the mode. The CR background gradient term also introduces an imaginary part that looks like damping. However, the more accurate interpretation of this term is that as the mode propagates down the CR pressure gradient, the perturbation amplitude normalized by the local CR pressure, $\delta p_c/p_c(z)$, remains constant.

Because streaming CRs heat the gas at a rate $-\chi \mathbf{v_A} \cdot \nabla p_c$, they also modify the gas-entropy mode by giving it a real (oscillatory) frequency, which at small η is $\omega \approx -4\eta\omega_{\rm A}/15$ (Kempski & Quataert 2020). Importantly, to leading order CR heating does not significantly affect the growth/damping of the gas-entropy mode (e.g. due to thermal instability), just its real frequency.

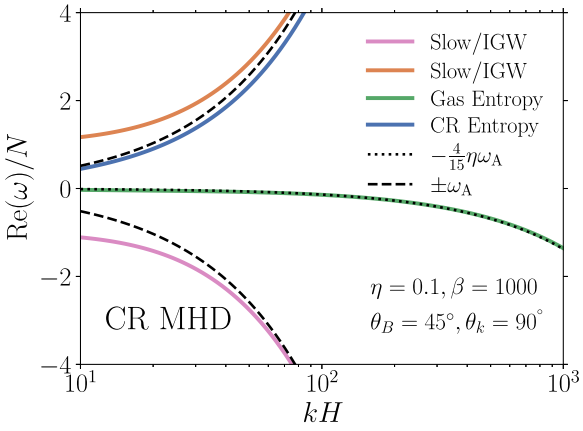

Figure 1. Oscillation frequencies of gravity/slow and entropy modes in stratified, collisional CR MHD. The frequencies are normalized by the Brunt–Väisälä frequency. Here, and in other figures (except Fig. 6), we use $\phi_k = 0$. The two modes that are characterized by the buoyancy frequency at long wavelengths (orange and pink lines) become the MHD slow magnetosonic modes at short wavelengths. The oscillation frequency of the gas-entropy mode (green line) is due to CR heating. The blue line shows the CR-entropy mode with frequency $\approx\omega_{\rm A}$, with the small deviation arising from finite η. We will show that gravity destabilizes the CR-entropy mode in low-collisionality MHD. We term this instability the CRBI.

We summarize the discussion above by showing the oscillation frequencies of gravity and entropy modes in stratified, collisional CR MHD in Fig. 1. The frequencies are normalized by the Brunt–Väisälä frequency. The two modes that are characterized by the buoyancy frequency at long wavelengths (orange and pink lines) become the MHD slow magnetosonic modes at short wavelengths. The gas-entropy mode (green line) is unaffected by buoyancy, and its oscillation frequency is due to CR heating. The blue line shows the CR-entropy mode with frequency $\approx\omega_{\rm A}$. Fig. 1 suggests that the CR-entropy mode is not significantly affected by buoyancy in collisional MHD. However, we will show that gravity destabilizes the mode in low-collisionality MHD (i.e. on small scales), which we term the CRBI.

3.2 Compressible CR entropy mode due to streaming

Surprisingly, the CR entropy mode becomes highly compressible at short wavelengths due to the influence of a finite mean free path in the background plasma, i.e. due to Δp (this is also true in a uniform background without stratification). At high β, pressure balance implies $\delta p_c + \delta p_\perp \approx 0$. In the isothermal limit due to rapid conduction (Pr $\ll 1$), such that to leading order $\delta p_\perp/p_g \sim \delta\rho/\rho$, and neglecting CR diffusion, this can be rewritten as (see equation (33)):

$$\frac{\delta\rho}{\rho} + \frac{\delta p_c}{p_g} = \frac{\delta\rho}{\rho} + \eta \frac{\frac{4}{3}\boldsymbol{k}\cdot\mathbf{v} - \frac{2}{3}\chi\omega_{\rm A}\frac{\delta\rho}{\rho} + \frac{1}{3}\beta\omega_{\rm A}\chi\frac{\delta\Delta p}{p_g}}{\omega - \chi\omega_{\rm A}} \approx 0. \quad (42)$$

In the limit of long wavelengths/high collisionality such that $\delta\Delta p$ is negligible, pressure balance is achieved if $\delta\rho/\rho \to 0$, i.e. $k_x {\rm v}_x + k_y {\rm v}_y + k_z {\rm v}_z = 0$ or $\boldsymbol{k}_\perp \cdot \mathbf{v}_\perp + k_\parallel {\rm v}_\parallel = 0$. This is the standard result that pressure-balanced modes are nearly incompressible at high β.

At shorter wavelengths and high β, the $\delta\Delta p/p_g$ term is dominant for the CR entropy mode with $\omega \approx \omega_{\rm A}$. Pressure balance then requires that the pressure anisotropy is minimized, $\delta\Delta p \approx 0$. This condition leads to the unusual requirement that the pressure-balanced mode is highly compressible. In Braginskii MHD $\Delta p \propto (2k_\parallel {\rm v}_\parallel - \boldsymbol{k}_\perp \cdot \mathbf{v}_\perp)$

so that equation (42) is satisfied when,

$$\boldsymbol{k}_\perp \cdot \mathbf{v}_\perp \approx 2k_\parallel \mathrm{v}_\parallel. \tag{43}$$

The exact relation satisfied by $\mathrm{v}_\perp$ and $\mathrm{v}_\parallel$ can be different in the collisionless regime, i.e. below the ion mean free path, where Braginskii MHD is no longer valid. However, the qualitative conclusion remains the same and the mode is very compressible. We next show how the pressure-balanced compressible mode is destabilized by gravity.

3.3 How gravity destabilizes the compressible CR entropy mode

To show how gravity destabilizes the compressible CR entropy mode discussed above, we consider a simple model in which we ignore magnetic tension and damping by anisotropic pressure (viscosity). As in Section 3.1, we consider the case $\boldsymbol{B} = B\hat{\boldsymbol{z}}$, $\boldsymbol{g} = -g\hat{\boldsymbol{z}}$, and consider a mode with $k_x \mathrm{v}_x = \alpha k_z \mathrm{v}_z$ imposed by pressure balance. As described in Section 3.2, $\alpha = -1$ in standard MHD, while $\alpha = 2$ in Braginskii MHD with CRs. The momentum equations are,

$$\omega \mathrm{v}_x = \frac{k_x}{\rho}\delta P_{\rm tot}, \tag{44}$$

$$\omega \mathrm{v}_z = \frac{k_z}{\rho}\delta P_{\rm tot} - i\omega_{\rm ff} c_s \frac{(1+\alpha)k_z \mathrm{v}_z}{\omega}, \tag{45}$$

where $\delta P_{\rm tot} = \delta p_\perp + \delta p_c + \delta(B^2/8\pi)$ is the total perturbed pressure. In the equation for v_z we used that $\omega\delta\rho/\rho \approx (1+\alpha)k_z\mathrm{v}_z$. Multiplying equation (44) by k_x and subtracting from equation (45) times αk_z, we find that

$$\frac{\delta P_{\rm tot}}{\rho}\left(\alpha k_z^2 - k_x^2\right) = i\alpha(1+\alpha)k_z c_s \omega_{\rm ff}\frac{k_z \mathrm{v}_z}{\omega}. \tag{46}$$

Using this expression for $\delta P_{\rm tot}$ back in equations (44) and (45) gives a simple dispersion relation:

$$\omega \approx \frac{1}{\sqrt{2}}(1+i)\left[(1+\alpha)k_z c_s \omega_{\rm ff}\frac{kx^2}{\alpha k_z^2 - k_x^2}\right]^{1/2} \sim \sqrt{\omega_s \omega_{\rm ff}}. \tag{47}$$

In this simplified picture gravity leads to growth rates that are of order $\sim \sqrt{\omega_{\rm ff}\omega_s} \gg \omega_{\rm ff}$. The above analysis can be easily repeated for the case $\boldsymbol{g} \perp \boldsymbol{B}$ (i.e. horizontal magnetic field in a vertical gravitational field), with very similar results. We stress that the scaling $\sim \sqrt{\omega_{\rm ff}\omega_s}$ in equation (47) does not describe compressible sound waves, which are approximately longitudinal at high β: $\alpha \approx k_x^2/k_z^2$ and the denominator in equation (47) is approximately zero.

Akin to standard buoyancy instabilities, the mode found here is destabilized by the unbalanced gravitational force acting on the mode's density fluctuations. However, in contrast to standard buoyancy instabilities, such as thermal convection in stars or the magneto-thermal instability (MTI; Balbus 2000) and the heat-flux-driven buoyancy instability (HBI; Quataert 2008) in clusters, the density fluctuations in the CR-driven instability are not due to the background stratification of the plasma. The density fluctuations at short wavelengths are instead due to CR streaming, independent of the background stratification.

In subsequent sections, we show that while magnetic tension does not affect the growth rate significantly, the effect of damping by anisotropic pressure should generally be retained. However, at sufficiently high β there is a range of scales for which the simple model considered in this section provides a good picture of the instability (see equation (51) below), and the growth rates are indeed $\sim \sqrt{\omega_s\omega_{\rm ff}}$. This regime is shown in Fig. 2. The solid black line shows the instability growth rate, computed from numerical solutions of the full set of linear equations in Section 2.5, as a function of wavenumber for $\beta = 10^7$, $\eta = 0.1$, $\boldsymbol{B}$ antiparallel to $\boldsymbol{g}$, and $k_x = k_z$. The 'x' markers show the growth rate for $\boldsymbol{B}$ perpendicular to $\boldsymbol{g}$ and $k_x = -k_z$. The dotted line labelled $\sim \sqrt{\omega_s\omega_{\rm ff}}$ shows the predicted growth rate from equation (47), which matches the exact solution very well over a wide range in k.

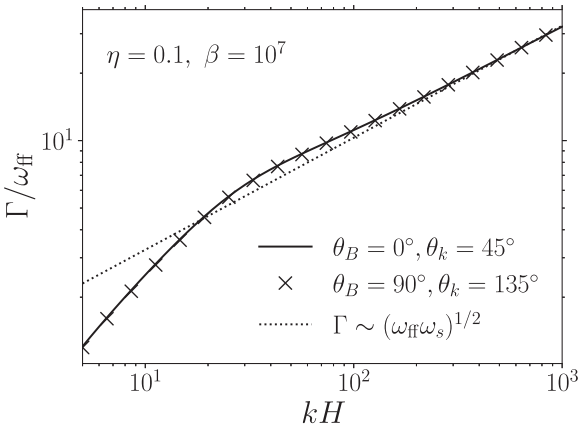

Figure 2. Growth rates of the CRBI for $\beta = 10^7$, $\eta = 0.1$, and $H = 1000 l_{\rm mfp}$. The angles θ_B and θ_k are the directions of $\boldsymbol{B}$ and $\boldsymbol{k}$ with respect to the positive z-direction ($\boldsymbol{g} = -g\hat{\boldsymbol{z}}$). At high β, damping by anisotropic pressure is negligible over a range of k and the instability is well-described by the simple model in Section 3.3. The dotted line labelled $\sim \sqrt{\omega_s\omega_{\rm ff}}$ shows the predicted growth rate from equation (47). This elucidates the physics of the CRBI in its simplest form. Figs 3–10 show results for more realistic ICM conditions.

We now discuss the instability in the astrophysically more relevant regimes where equation (47) is not as accurate.

4 DISPERSION RELATION AND GROWTH RATES OF SHORT-WAVELENGTH MODES

In Section 3.3, we neglected damping by anisotropic pressure (viscosity), which generally changes the growth rates relative to those predicted in equation (47) (except for certain asymptotic limits, e.g. very large β as in Fig. 2). In this section, we present a more accurate calculation and derive an approximate dispersion relation.

For simplicity, we here ignore background gradient terms (i.e. we set BG = 0 in equations (27)–(33)) in our analytic derivation of the growth rates. Ignoring background gradients is a reasonable simplification because we find that short-wavelength modes (which are the fastest growing modes) are not significantly affected by explicitly including background gradients (even though they should formally be included). This is because the CRBI is due to streaming-induced compressibility and not background stratification.[2] This is in contrast to thermal convection in stars or the MTI/HBI in clusters, which are driven by heat conduction and background temperature gradients. Our analytic results from this section will be supplemented by numerical solutions of the full system of linearized equations (equations (27)–(33)) including background gradients in Section 5.

[2]However, we note that a non-zero CR pressure gradient along the magnetic field is generally necessary for equilibrium and to couple CRs to the thermal gas.

4.1 Dispersion relation

In this section, it is convenient to work in a coordinate system aligned with the magnetic field: $\boldsymbol{B} = (0, 0, B)$, $\boldsymbol{k} = (k_\perp, 0, k_\parallel)$, and $\boldsymbol{g} = (g_{\perp;1}, g_{\perp;2}, g_\parallel)$. In this coordinate system, and if we neglect background-gradient terms (which we do here), Alfvénic fluctuations of the form $\boldsymbol{\delta B} = (0, \delta B, 0)$ and $\boldsymbol{\delta v} = (0, \delta v, 0)$ decouple, which leaves velocity/magnetic field fluctuations in the $\boldsymbol{k} - \boldsymbol{B}$ plane for the remaining modes. If background gradients are kept, this is strictly true only if gravity is coplanar with $\boldsymbol{k}$ and $\boldsymbol{B}$. In the high-β and isothermal limit ($\omega_{\rm cond} \gg \omega$), the third order dispersion relation for the slow-magnetosonic and CR-entropy modes can be found by crossing the momentum equation (28) twice with $\boldsymbol{k}$, taking the component parallel to $\boldsymbol{B}$ and using equation (42):

$$0 = \omega^2\left(\frac{2}{3}i\chi\eta\frac{\omega_B}{\omega_{\rm A}}\omega(2k_\parallel^2 - k_\perp^2) + k^2\Delta\right) + 3ik_\perp^2\omega_B\omega\Delta + 2\chi\eta\frac{\omega_B}{\omega_{\rm A}}k_\parallel\omega_{\rm ff}c_s\omega\left(-k^2(\hat{\boldsymbol{b}}\cdot\hat{\boldsymbol{g}}) + (\boldsymbol{k}\cdot\hat{\boldsymbol{g}})k_\parallel\right) - \omega_{\rm A}{\rm v}_{\rm A}k^2k_\parallel\left(\frac{4}{3}i\eta\chi\frac{\omega_B}{\omega_{\rm A}}\omega + \Delta\right), \quad (48)$$

where,

$$\Delta = \omega - \chi\omega_{\rm A} + i\omega_d + \frac{4}{3}\eta\omega - \frac{2}{3}\eta\chi\omega_{\rm A}. \quad (49)$$

The three solutions of the cubic dispersion relation in equation (48) are the two slow magnetosonic waves and the CR entropy mode. The gas entropy mode is not present because our calculation assumed that modes are isothermal, $\delta p_g/p_g = \delta\rho/\rho$, which eliminates the gas entropy mode (i.e. the gas entropy equation acts as a constraint). The first term in equation (48) comes from crossing the velocity perturbation twice with $\boldsymbol{k}$, the second term is the damping by Braginskii viscosity, the third term is the gravitational force, and the last term comes from the perturbed magnetic tension. We note that the gravitational force term, which drives the instability, is zero if $\boldsymbol{g}$ is perpendicular to the $\boldsymbol{k} - \boldsymbol{B}$ plane.

As explained in Section 3.3, the instability is driven by gravity mediated by compressibility induced by CR streaming. The compressibility is a consequence of the perturbed pressure anisotropy $\delta\Delta p$, characterized by the Braginskii viscous frequency $\omega_{\rm B}$, in the CR entropy equation. This suggests that compressibility effects are most important in the short-wavelength limit $\omega_B/\omega_{\rm A} \gg 1$. In this limit, the dispersion relation can be simplified to

$$0 = \omega^2\frac{2}{3}i\chi\eta\frac{\omega_B}{\omega_{\rm A}}\left(2k_\parallel^2 - k_\perp^2\right) + 3ik_\perp^2\omega_B\Delta + 2\chi\eta\frac{\omega_B}{\omega_{\rm A}}k_\parallel\omega_{\rm ff}c_s\left(-k^2(\hat{\boldsymbol{b}}\cdot\hat{\boldsymbol{g}}) + (\boldsymbol{k}\cdot\hat{\boldsymbol{g}})k_\parallel\right) - \omega_{\rm A}{\rm v}_{\rm A}k^2k_\parallel\frac{4}{3}i\eta\chi\frac{\omega_B}{\omega_{\rm A}}. \quad (50)$$

4.2 Growth rates of short-wavelength modes

We split the eigenmode frequency into real and imaginary parts, $\omega = \omega_{\rm R} + i\Gamma$, such that $\Gamma > 0$ corresponds to exponential growth. We note that if magnetic tension and damping by pressure anisotropy in equation (50) can be ignored (fourth and second term, respectively), we recover the growth rate that was derived in Section 3.3, i.e. $\Gamma \sim \sqrt{\omega_s\omega_{\rm ff}}$. From equation (50), we see that damping by anisotropic viscosity (pressure) can be ignored if the third term $\propto \omega_{\rm ff}$ is much larger than the damping term, or

$$\beta \gg \eta^{-2}\left(\frac{\omega_s}{\omega_{\rm ff}}\right). \quad (51)$$

At sufficiently high β there is therefore a finite range of scales where the simple model from Section 3.3 and equation (47) correctly predict the solution (see Fig. 2).

We proceed by solving equation (50) in the limit $\eta \ll 1$, i.e. for small CR pressure fractions. To leading order, $\Delta = 0$ is a solution, which, ignoring CR diffusion, implies

$$\omega \approx \chi\omega_{\rm A}. \quad (52)$$

This mode is the CR entropy mode. We stress again that the dependence on $\omega_{\rm A}$ in the CR entropy mode does not come from the perturbed magnetic tension, but from CR streaming along field lines at the Alfvén speed, which also has characteristic frequency $\omega_{\rm A}$. The growth rate of the mode can be found at first order in η and is approximately given by,

$$\Gamma \approx \chi\frac{\sqrt{2}}{3}\eta\beta^{1/2}\omega_{\rm ff}\frac{-k^2\hat{\boldsymbol{b}}\cdot\hat{\boldsymbol{g}} + \boldsymbol{k}\cdot\hat{\boldsymbol{g}}k_\parallel}{k_\perp^2}, \quad (53)$$

where $\chi = \pm1$ is the parameter that ensures that CR stream down their pressure gradient (equation (10)). The growth rate increases with increasing β, as at higher β the pressure anisotropy is better minimized (equation (42)) and anisotropic viscous damping is reduced. There is no unstable growth if gravity is normal to the $\boldsymbol{k} - \boldsymbol{B}$ plane. In the case of a magnetic field that is antiparallel to $\boldsymbol{g}$,

$$\Gamma \sim \chi\eta\beta^{1/2}\omega_{\rm ff}, \quad \boldsymbol{B} = B\hat{\boldsymbol{z}},\ \boldsymbol{g} = -g\hat{\boldsymbol{z}}. \quad (54)$$

For a horizontal magnetic field along x,

$$\Gamma \sim -\chi\eta\beta^{1/2}\omega_{\rm ff}\frac{k_zk_x}{k_z^2 + k_y^2}, \quad \boldsymbol{B} = B\hat{\boldsymbol{x}},\ \boldsymbol{g} = -g\hat{\boldsymbol{z}}. \quad (55)$$

While for $\boldsymbol{B} = B\hat{\boldsymbol{z}}$ and $\chi > 0$ all modes are unstable (except when $\boldsymbol{k}$ is approximately parallel to or perpendicular to $\boldsymbol{B}$), for $\boldsymbol{B} = B\hat{\boldsymbol{x}}$ growth occurs if $\chi k_xk_z < 0$. Unless $\boldsymbol{B} \parallel \boldsymbol{g}$ and $\chi\boldsymbol{B}\cdot\boldsymbol{g} > 0$ ($dp_c/dz > 0$, which is unlikely), there exists a region in k-space where there is wave growth. We note that for horizontal magnetic fields growth rates can be higher than for vertical magnetic fields because of the extra factor that depends on the direction of propagation, although growth rates with $k_x \gg k_y$, k_z do not diverge because the ordering used to derive equations (53)–(55) breaks down.

The above solutions are for pure CR streaming and also do not include the impact of background gradients on the growth rates. By neglecting CR diffusion we have assumed that CRs are perfectly coupled to the self-excited Alfvén waves and so stream at the Alfvén speed. We include CR diffusion in our analysis to relax the assumption of pure Alfvénic streaming, which certainly breaks down on small scales. From equation (48), or from the fact that in the presence of diffusion the CRs' natural frequency is $\omega \approx \omega_{\rm A} - i\omega_d$ (see equation (41)), we can estimate that CR diffusion suppresses the instability when

$$\omega_d \gtrsim \eta\beta^{1/2}\omega_{\rm ff} \quad (56)$$

or equivalently

$$kl_{\rm mfp} \gtrsim \left(\Phi^{-1}\frac{l_{\rm mfp}}{H}\eta\beta^{1/2}\right)^{1/2}, \quad (57)$$

where we used the parameter Φ defined in equation (21).

Equation (41) also allows us to estimate how background gradients affect the growth rate in equation (53). The background CR pressure gradient modifies the mode's imaginary part by ${\rm v}_{{\rm A},z}d\ln p_c/dz \sim {\rm v}_{{\rm A},z}/H \sim \omega_{\rm ff}/\beta^{1/2}$, which encapsulates that as the perturbation propagates down the CR pressure gradient, $\delta p_c/p_c(z)$ remains constant in collisional MHD without CR diffusion. The background therefore

significantly modifies the growth rate if,

$$\frac{\omega_{\rm ff}}{\beta^{1/2}} \gtrsim \eta\beta^{1/2}\omega_{\rm ff} \implies \eta \lesssim \beta^{-1}. \quad (58)$$

We stress again that for $\eta \lesssim \beta^{-1}$ the mode is not damped in the usual sense, because it maintains approximately constant $\delta p_c/p_c(z)$ as it propagates down the CR pressure gradient.

5 CRBI IN AN ISOTHERMAL ATMOSPHERE

We now complement the analytics of Section 4 with numerical solutions of equations (27)–(33) including background gradients. In this section, we consider an isothermal atmosphere in order to isolate the CRBI from the HBI/MTI, which require background temperature gradients. As our fiducial set of parameters, we use $\eta = 0.1$, $\beta = 100$, and $H = 100 l_{\rm mfp}$. The background is in the hydrostatic equilibrium described by equations (25) and (26). We assume that the background CR heating is balanced by an unspecified cooling function, which we do not perturb in our linear analysis, except in Section 6.2 (see Kempski & Quataert 2020 for a discussion of thermal instability with streaming CRs). Unless specified otherwise, we will consider wavevectors $\boldsymbol{k}$ in the $\boldsymbol{B} - \boldsymbol{g}$ plane, i.e. $\phi_k = 0$ (see Section 2.5), motivated by the fact that the instability is not present if $\boldsymbol{g}$ is perpendicular to the $\boldsymbol{B} - \boldsymbol{k}$ plane. We show how growth rates depend on ϕ_k in Fig. 6.

The physics of the instability described in Section 3 becomes apparent by plotting the properties of the CRBI. We show the mode properties for $\eta = 0.1$ and $\beta = 100$ in Fig. 3. We plot the oscillation frequency in panel (a), the growth rate in panel (b), $k_\parallel \mathrm{v}_\parallel / k_\perp \mathrm{v}_\perp$, which quantifies the compressibility of the mode (=−1 if incompressible), in panel (c), and $[\delta p_c + \delta(B^2/8\pi)]/\delta p_g$, which quantifies the degree of pressure balance (=−1 if pressure balanced, i.e. $\delta p_c + \delta(B^2/8\pi) + \delta p_g = 0$), in panel (d). The blue line shows the unstable CR entropy mode. For completeness, we also plot the MHD slow modes and the gas-entropy mode. Panel (b) shows that all modes except the CR entropy mode are strongly damped by low-collisionality physics (viscosity and conduction). At small k, the CR entropy mode is approximately incompressible ($k_\parallel \mathrm{v}_\parallel \approx -k_\perp \mathrm{v}_\perp$) and the growth rates are $\ll \omega_{\rm ff}$. At high k, the mode becomes compressible due to CR streaming, approaches $k_\perp \mathrm{v}_\perp = 2k_\parallel \mathrm{v}_\parallel$, and the growth rate reaches the plateau given by equation (53). We note that $k_\perp \mathrm{v}_\perp$ does not quite reach $2k_\parallel \mathrm{v}_\parallel$ because we limit the x-axis to $k l_{\rm mfp} < 1$, where the Braginskii MHD model is valid. The oscillation frequency $\approx \omega_A$ is set by the characteristic frequency of CR streaming.

In Fig. 4, we show growth rates of the CRBI for the fiducial parameters and different ratios of CR pressure to gas pressure, η. The instability exists even for small CR pressures, but with reduced growth rates. In the analytics in Section 4 without background gradients, the instability exists for arbitrarily small CR pressures. Here, we find that with background gradients, within our local WKB framework, the instability exists for any $\eta \gtrsim \beta^{-1}$ (ignoring CR diffusion), which is consistent with the discussion at the end of Section 4.2. However, we stress that because for very small η (e.g. $\eta = 0.025$ in Fig. 4) the mode's e-folding distance is generally of order or larger than the background scale height (if $\Gamma/\omega_{\rm ff} \lesssim \beta^{-1/2}$), a more general treatment than our local WKB approach would be valuable to study the overstability in this parameter range. We show the number of e-folds $N_{\rm e}$ generated by the CRBI during one scale-height-crossing time as a function of η in Fig. 5. We use that the mode propagates along the magnetic field at approximately the Alfvén speed (equation (52); this is correct to a very good approximation at small η, for $\eta \sim 1$ the real frequency is ~ 20 per cent less than predicted by equation

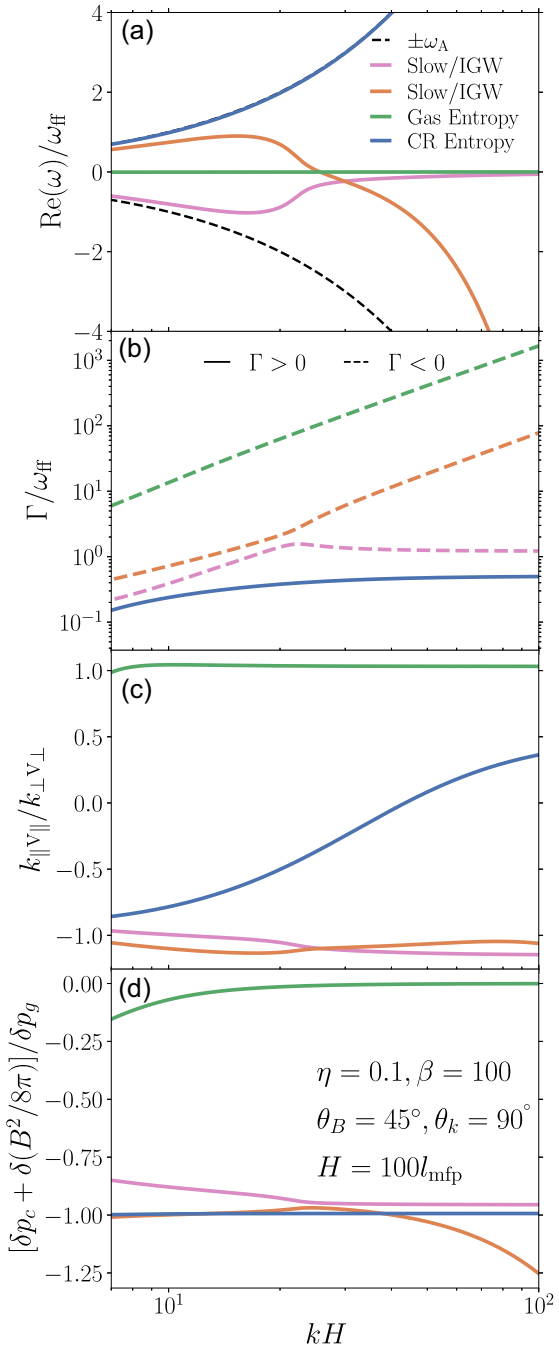

Figure 3. Mode properties for $\eta = 0.1$, $\beta = 100$, and $H = 100 l_{\rm mfp}$. $\theta_B = 45°$ and $\theta_k = 90°$ are the directions of $\boldsymbol{B}$ and $\boldsymbol{k}$ with respect to $\hat{\boldsymbol{z}}$ ($\boldsymbol{g} = -g\hat{\boldsymbol{z}}$), while $\perp$ and $\parallel$ are defined w.r.t. $\boldsymbol{B}$. We plot oscillation frequencies in panel (a), growth rates in (b) ($\Gamma > 0$ corresponds to growth), $k_\parallel \mathrm{v}_\parallel / k_\perp \mathrm{v}_\perp$, which quantifies the compressibility of the mode, in (c), and $[\delta p_c + \delta(B^2/8\pi)]/\delta p_g$, which quantifies the degree of pressure balance, in (d). The blue line shows the unstable CR entropy mode, the orange and pink lines are the MHD slow modes, and the green line is the gas-entropy mode. All modes except the CR entropy mode are damped by low-collisionality effects. Long-wavelength CR entropy modes are approximately incompressible and the growth rates are small. High-k CR entropy modes become compressible due to CR streaming while maintaining pressure balance, and the growth rate reaches the plateau given by equation (53).

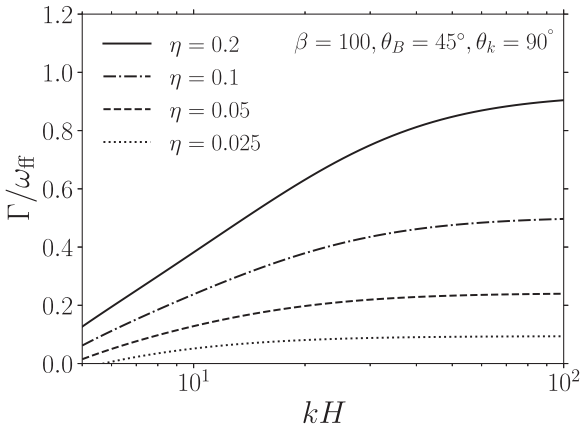

Figure 4. Growth rates of the CRBI for $\beta = 100$, $H = 100 l_{\rm mfp}$, and different ratios of CR pressure to gas pressure, η. The other parameters are set to the fiducial values (Section 5). The angles $\theta_B = 45°$ and $\theta_k = 90°$ are the directions of $\boldsymbol{B}$ and $\boldsymbol{k}$ with respect to the positive z-direction ($\boldsymbol{g} = -g\hat{\boldsymbol{z}}$). Even at very small CR pressures (small η), the instability still exists in our local analysis (see main text for more discussion), but with reduced growth rates (equation (53)).

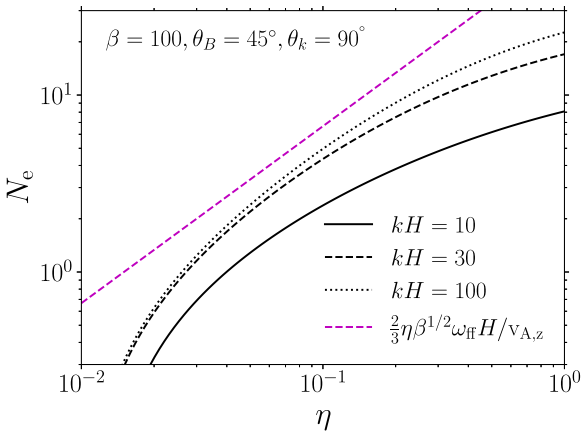

Figure 5. Number of e-folds, N_e, generated by the CRBI in the time it takes the mode to propagate one scale height in the vertical direction, as a function of η and for selected values of kH. Here we use $\beta = 100$, $\theta_B = 45°$, and $\theta_k = 90°$. We use equation (52), i.e. that the mode propagates at the Alfvén speed along the magnetic field (this is correct to a very good approximation at small η, with ~ 20 per cent deviations for $\eta \sim 1$). The magenta dashed line uses the growth rate from equation (53), which assumes small η and does not take into account background gradients (which decrease the growth rate in our local analysis, see discussion at the end of Section 4.2). The black lines use growth rates computed numerically from equations (27) to (33). It is worth noting that for parameters which yield $N_{\rm e} \lesssim 1$ (here $\eta \lesssim 0.05$) the CRBI does not result in significant amplification over one scale-height-crossing time. The local WKB method we use to study the CRBI is most reliable for $N_{\rm e} \gg 1$.

(52)). Our WKB results are most reliable for parameters which yield $N_{\rm e} \gg 1$.

We show growth rates as a function of propagation direction at fixed $kH = 20$ in Fig. 6 for different orientations of the background magnetic field. The growth rates in the three panels have a qualitatively different angular dependence, consistent with equations (54) and (55). For horizontal magnetic fields growth rates are larger than for vertical magnetic fields, but growth occurs in a smaller region of k-space.

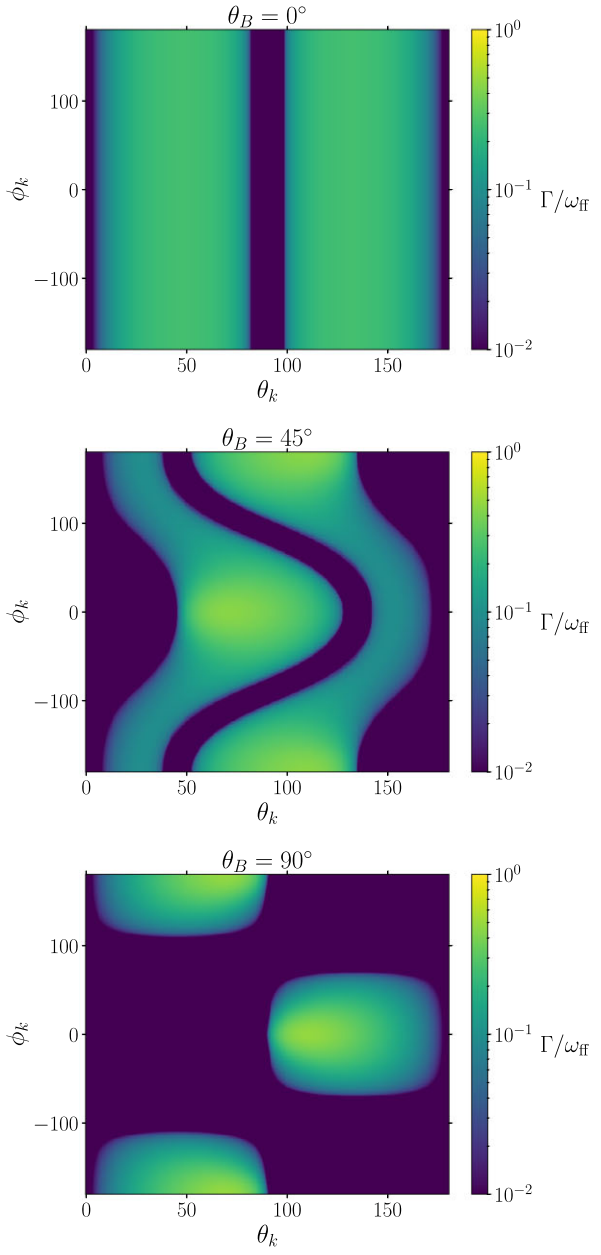

Figure 6. CRBI growth rates as a function of propagation direction for $\eta = 0.1$, $\beta = 100$, $H = 100 l_{\rm mfp}$, and fixed $kH = 20$. The angles θ_k and ϕ_k are defined such that $k_x = k\sin\theta_k\cos\phi_k$, $k_y = k\sin\theta_k\sin\phi_k$, and $k_z = k\cos\theta_k$ (all the other figures in this paper use $\phi_k = 0$). The three panels show growth rates for different orientations of the background magnetic field relative to gravity, which is in the $-\hat{\boldsymbol{z}}$ direction. The growth rates have a qualitatively different angular dependence for the different field geometries (see equations (53)–(55)).

In Section 4.2, we noted that significant CR diffusion suppresses the CRBI at short wavelengths. We now show this explicitly in Fig. 7 for different values of Φ, which quantifies the strength of CR diffusion (equation (21)).[3] As predicted by equation (57), diffusion suppresses the instability at high k.

[3]We assume that CR diffusion does not affect the background equilibrium, i.e. we assume an approximately linear CR pressure profile, $\kappa d^2 p_c/dz^2 \approx 0$.

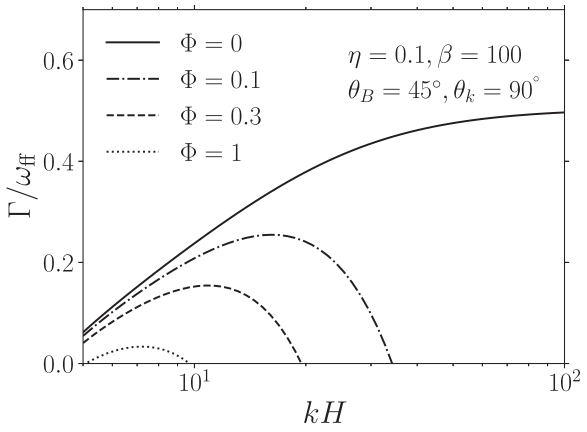

Figure 7. CRBI growth rates as a function of wavenumber and the CR diffusion coefficient (quantified using the parameter Φ defined in equation (21)). We assume $\eta = 0.1$, $\beta = 100$, $H = 100 l_{\rm mfp}$, and the isothermal background described in Section 5. CR diffusion suppresses growth at high k (equation (57)) and can completely shut off the instability if sufficiently large (equation (59)).

Given that the CRBI typically becomes important on scales $kH \gg 1$ and that at longer wavelengths buoyancy instabilities such as the HBI and MTI are generally more important (see Section 6.1 and Fig. 8), we can rephrase equation (57) in terms of a rough overall criterion for the suppression of the CRBI by CR diffusion (however, we note that for large thermal mean free paths, as in cluster outskirts, the CR-driven instability is important on scales $kH \sim 1$, see Fig. 10). Setting $k_{\rm min}H$ as the largest scale on which the CRBI operates and using equation (57), we find that CR diffusion suppresses the instability if,

$$\Phi \gtrsim 0.01 \eta \beta^{1/2} \frac{H}{l_{\rm mfp}} \left(\frac{k_{\rm min} H}{10} \right)^{-2}. \tag{59}$$

For $\eta = 0.1$, $\beta = 100$, $k_{\rm min}H = 10$, and $H = 100 l_{\rm mfp}$, CR diffusion suppresses the instability for $\Phi \gtrsim 1$, roughly consistent with Fig. 7.

6 DISCUSSION

6.1 CRBI versus HBI/MTI

We now consider the relationship between the CRBI and previously identified buoyancy instabilities driven by background temperature gradients and heat fluxes, i.e. the MTI (Balbus 2000) and the HBI (Quataert 2008). How CRs may affect these buoyancy instabilities has been considered in previous work (e.g. Chandran & Dennis 2006; Dennis & Chandran 2009; Sharma et al. 2009). However, they did not use streaming CR transport and so the CRBI was not included in their calculation.

Instead of an isothermal atmosphere as in Section 5, we here consider a background temperature that increases with height, as is the case in cluster cores:

$$\frac{d}{dz}(p_g + p_c) = -\rho g, \quad p_c \propto \rho^{2/3}, \quad \frac{d \ln T}{dz} = H^{-1}, \tag{60}$$

where $H = c_s^2/g = c_s/\omega_{\rm ff}$. This equilibrium with vertical magnetic field and T increasing with height is unstable to the HBI at high β (driven by the background anisotropic heat flux). We also consider a background with $dT/dz < 0$ and a horizontal magnetic field, $\boldsymbol{B} = B\hat{\boldsymbol{x}}$, which is unstable to the MTI. To study the MTI we consider the following background,

$$\frac{dp_g}{dz} = -\rho g, \quad \rho = \text{const}, \quad \frac{d \ln T}{dz} = -H^{-1} = -\frac{\omega_{\rm ff}}{c_s}. \tag{61}$$

For the MTI, we assume that $|\hat{\boldsymbol{b}} \cdot \nabla p_c|/p_c \ll H^{-1}$, so that the CRs are coupled but their background gradient is sufficiently small to be ignored (which is consistent with our choice of $\rho \approx$ const). We stress that this choice is made for the sake of simplicity and is not necessarily representative of cluster conditions.

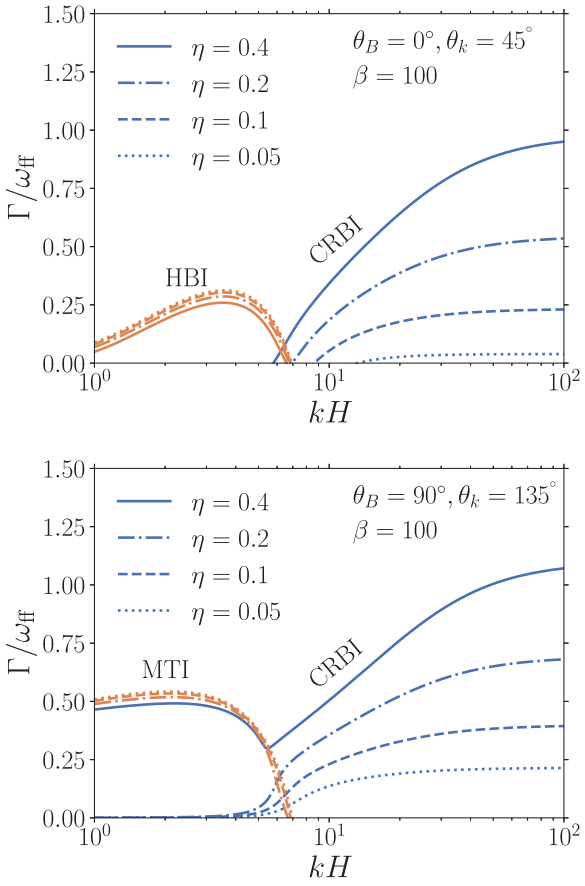

Figure 8. CRBI versus buoyancy instabilities driven by background stratification and anisotropic heat conduction, the HBI (top) and MTI (bottom). We use $\beta = 100$, $H = 100 l_{\rm mfp}$, and different η. Long-wavelength modes are destabilized by thermal conduction, as in the MTI/HBI. Short-wavelength modes are stable to the HBI/MTI due to the stabilizing effect of magnetic tension. Short-wavelength modes are, however, destabilized by the compressibility induced by CR streaming. The CRBI therefore operates alongside the long-wavelength HBI and MTI. For $\eta = 0.4$, the CRBI and the MTI are destabilizing the same mode (also true for the HBI at higher β).

We show growth rates for the backgrounds described by equations (60) and (61) in Fig. 8, for $\beta = 100$, $H/l_{\rm mfp} = 100$, and different values of η. We include $kH \sim 1$ in Fig. 8 to show HBI/MTI growth rates, although we note that our WKB approach is not rigorous in this wavelength regime. At small k, growth rates are dominated by the HBI/MTI. At high k, the HBI is partially stabilized by anisotropic viscosity (Kunz 2011), and the MTI and HBI are completely suppressed by magnetic tension. The HBI is also partially suppressed by the CR pressure gradient at long wavelengths (for large η), where CRs are approximately adiabatic, $\omega_{\rm A} < \omega_{\rm ff}$ (Sharma et al. 2009). Short-wavelength modes are destabilized by compressibility induced by CR streaming. We note that in the top panel there is a

range of wavelengths where our calculation does not predict unstable growth at small η, which is not the case in the bottom panel. This is due to the effect of the background CR pressure gradient on the growth rate, explained in Section 4.2, which is not present in the equilibrium used to study the MTI (equation (61)). Finally, we note that for $\eta = 0.4$ the CRBI and the MTI are in fact driving the same mode (this is also true for the HBI for β slightly larger than used in Fig. 8).

The CRBI considered in this work therefore operates alongside standard buoyancy instabilities driven by background gradients, such as the HBI/MTI. Both types of instabilities are driven by gravity acting on density fluctuations. At long wavelengths, for which the HBI/MTI operate, the density fluctuations that introduce unstable buoyancy are due to a combination of background density stratification, rapid heat conduction and pressure balance. At short wavelengths, the unstable density fluctuations are due to CR streaming and pressure balance, independent of the background stratification.

The transition from heat-flux-driven growth to CR-driven growth in Fig. 8 occurs around $kH \sim 5$. The exact value is sensitive to our choice of parameters, such as η or β. It also depends strongly on the thermal mean free path, more specifically the ratio $H/l_{\rm mfp}$, which sets the range of k for which CR streaming drives the mode away from incompressibility. In particular, for $H \sim l_{\rm mfp}$ the CRBI can have faster growth rates than the HBI/MTI at long wavelengths (see Fig. 10) for plausible parameters. We discuss the dependence of the CRBI on the value of the thermal particle mean free path in more detail in Section 6.3.

6.2 Impact of cooling

We have ignored cooling throughout this work. Given that the unstable short-wavelength CR entropy modes have significant density fluctuations due to CR streaming, cooling could in principle have an impact on the instability. However, because the unstable wavelengths are characterized by thermal-conduction times that are much shorter than the cooling time, the dominant response of the gas is simply that it is isothermal, even in the presence of cooling and large CR-driven density fluctuations. The perturbed cooling therefore has no significant effect on the CRBI even when the cooling rate ω_c is comparable to the growth rate, as we show in Fig. 9.

6.3 Dilute cluster outskirts and the collisionless regime

In Figs 3–9, we used a fixed $H/l_{\rm mfp} = 100$. While $H/l_{\rm mfp} \gg 1$ is representative of the conditions in the inner regions of galaxy clusters, $H/l_{\rm mfp}$ is likely smaller in the outskirts, where the ICM plasma density is significantly reduced. A larger mean free path implies that CR-streaming-induced compressibility effects become important on larger scales; the growth rates of long-wavelength modes will thus be enhanced relative to the results from Figs 3–9.

Considering a larger mean free path runs into the issue that the range of scales for which both the Braginskii MHD model and the WKB approximation are valid ($kl_{\rm mfp} \ll 1$ and $kH \gg 1$, respectively) becomes very limited. To alleviate this issue, we here consider a different model for the low-collisionality thermal plasma. We use the kinetic MHD equations (Chew, Goldberger & Low 1956) with a 'Landau-fluid' prescription for the heat fluxes, i.e. the heat fluxes are constrained by the requirement that the fluid equations approximately match the linear response of the kinetic thermal plasma (Snyder, Hammett & Dorland 1997). We use the heat fluxes from Snyder et al. (1997) that depend on the collision rate, allowing for a smooth

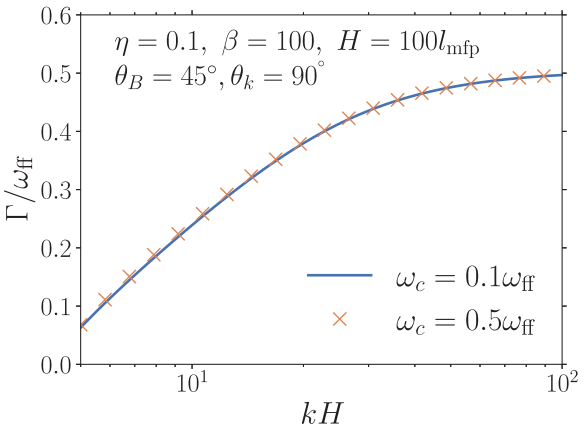

Figure 9. Growth rates of the CRBI are not significantly affected by cooling even when the cooling rate ω_c is comparable to the growth rate. This is because the mode is isothermal due to rapid conduction (the wavelengths shown are below the Field length where thermal instability is suppressed by conduction; Field 1965). For this plot, we assume thermal Bremsstrahlung to be the dominant radiative cooling process.

transition between the weakly collisional (Braginskii MHD) and collisionless regimes. The equations of the Landau-fluid model are provided in Appendix A. For simplicity, we ignore electron physics and only consider the thermal ions, which dominate the pressure anisotropy because the ion collision rate is much smaller than the electron collision rate. Ignoring the effect of the electron heat flux on the ions is generally not rigorous (in our Braginskii calculation the heat flux was due to electrons, hence Pr = 0.02). However, as discussed in Section 2.3.1, the electron-ion thermal equilibration rate is $\tau_{\rm eq}^{-1} \sim (m_e/m_i)^{1/2}\nu_{\rm ii} \sim \nu_{\rm ii}/40$, i.e. ions and electrons are thermally decoupled for $\omega \sim \omega_{\rm A}$ modes if $kl_{\rm mfp} \gg \beta^{1/2}/40$. For $\beta \sim 100$ and $kl_{\rm mfp} \gtrsim 1$ electrons and ions are then approximately thermally decoupled. It is therefore reasonable to neglect the electron heat flux in the collisionless regime, which is of primary interest in this section.

We show growth rates of the CRBI, calculated using the Landau-fluid model (black lines), in Fig. 10 for $\eta = 0.1$, $\beta = 100$, and different $H/l_{\rm mfp}$. As expected, for larger $l_{\rm mfp}$ the growth rates of long-wavelength modes are enhanced, as CR streaming leads to larger density fluctuations on large scales. The asymptotic growth rate at high k is independent of the mean free path (absent CR diffusion). We also compare the Landau-fluid results to the Braginskii MHD calculation for the fiducial case $H/l_{\rm mfp} = 100$ (solid line and magenta crosses in Fig. 10). There is good agreement between the two models in the collisional regime, which shows that instability growth rates are not very sensitive to the thermal Prandtl number, as the Braginskii MHD model has Pr = 0.02 while the Landau-fluid model has Pr $\sim$ 1 (this is consistent with our finding that Pr = 0.02 and Pr $\sim$ 1 yield similar results in Braginskii MHD). The asymptotic high-k growth rates in the two models are also remarkably similar. This is because the qualitative physical picture of the instability does not change between the collisional and collisionless regimes (although the exact relationship satisfied by $k_\parallel v_\parallel$ and $k_\perp v_\perp$ at high k is different in the two models, and in the Landau-fluid model $k_\parallel v_\parallel \gg k_\perp v_\perp$).

6.4 Diffusive correction to CR streaming

Fig. 7 shows that significant CR diffusion can suppress the CRBI. The magnitude of the diffusive correction to Alfvénic streaming is therefore critical. The diffusive correction depends on the damping

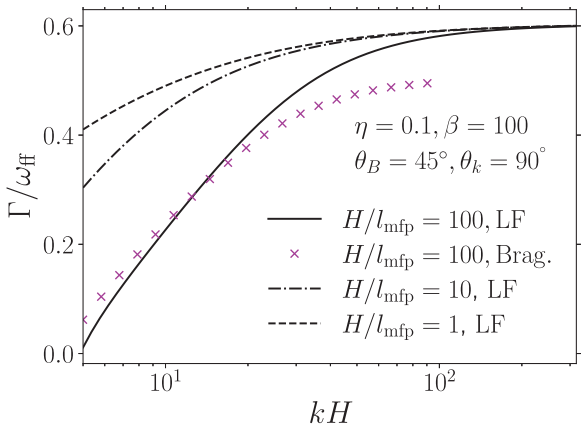

Figure 10. Growth rates of the CRBI, calculated using the Landau-fluid model (black lines), for $\eta = 0.1$, $\beta = 100$, and different $H/l_{\rm mfp}$. The Landau-fluid model allows us to compute approximate growth rates for both the collisional and collisionless regimes. For larger $l_{\rm mfp}$, as is likely the case in dilute cluster outskirts, the growth rates of long-wavelength modes are enhanced, as CR streaming leads to significant density fluctuations on large scales. There is good agreement between Landau-fluid and Braginskii MHD (magenta crosses) predictions in the collisional regime, as expected.

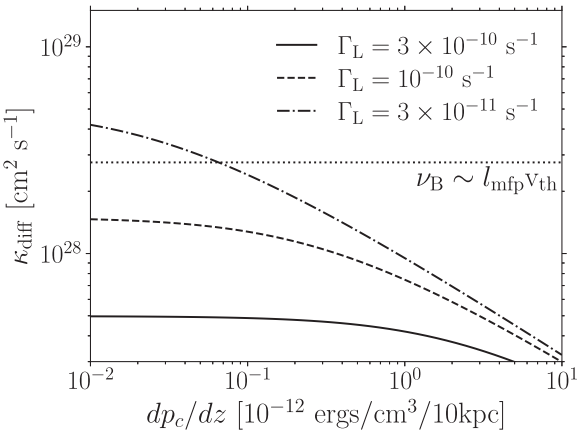

Figure 11. The diffusive correction to Alfvénic streaming calculated from equation (B2) as a function of the CR pressure gradient, for different magnitudes of the linear damping of Alfvén waves excited by the CR streaming instability. The horizontal dotted line is the anisotropic viscosity of the thermal gas for $l_{\rm mfp} \sim 0.2$ kpc and $T = 3 \times 10^7$ K. Thus, $\Phi < 1$ (see equation (21)) is plausible in cluster cores and the CRBI is likely only partially suppressed by CR diffusion (Fig. 7).

of the Alfvén waves excited by the CR streaming instability. In the ICM, the dominant damping mechanisms are non-linear Landau damping $\sim k {\rm v_{th}} (\delta B/B)^2$ (Lee & Völk 1973; Kulsrud 2005) and linear Landau damping of Alfvén waves in a turbulent background (Wiener, Zweibel & Oh 2018). For turbulence injected on $\sim$10 kpc (a common scale for the radio bubbles) with perturbations comparable to the Alfvén speed, the linear-Landau damping rate of $k \sim r_L^{-1}$ Alfvén waves excited by GeV CRs (where r_L is the GeV CR gyroradius) is

$$\Gamma_{\rm L} \sim \frac{0.4 {\rm v_{th}}}{(r_L L_{\rm turb})^{1/2}} \sim 10^{-10}\ {\rm s}^{-1} \frac{{\rm v_{th}}}{10^8 {\rm cm\ s}^{-1}} \left(\frac{L_{\rm turb}}{10\ {\rm kpc}}\right)^{-1/2} \left(\frac{B}{1\ \mu{\rm G}}\right)^{1/2}. \quad (62)$$

We compute the correction to Alfvénic streaming for a combination of linear and non-linear damping mechanisms in Appendix B. The resulting diffusion coefficient is a function of the background CR pressure gradient. We split the total diffusion coefficient κ into two components, $\kappa(\nabla p_c) = \kappa_{\rm diff}(\nabla p_c) + \kappa_{\rm st}(\nabla p_c)$, where $\kappa_{\rm st}$ is the part of the diffusion coefficient that scales as $\kappa_{\rm st} \propto (\nabla p_c)^{-1}$ and therefore does not result in real diffusive behaviour (as needed to suppress the CRBI). For purely linear damping mechanisms, $\kappa = \kappa_{\rm st}$ (Skilling 1971). Diffusive behaviour in the form of a finite $\kappa_{\rm diff}$ comes from non-zero non-linear damping.

$\kappa_{\rm diff}$ is plotted for different linear damping strengths in Fig. 11 as a function of the CR pressure gradient, normalized using $p_c = 10^{-12}$ erg cm^{-3} and a scale height $H_c = 10$ kpc. In addition to linear damping, the waves excited by the streaming instability are damped by non-linear Landau damping. We plot $\kappa_{\rm diff}$ rather than the total $\kappa = \kappa_{\rm diff} + \kappa_{\rm st}$ because $\kappa_{\rm diff}$ is the component that acts as a diffusion term (see Appendix B). The non-diffusive correction to Alfvénic streaming $\kappa_{\rm st}$ likely does not suppress the CRBI and is a small correction to Alfvénic streaming for the GeV CRs in a steady state (Kempski & Quataert 2022).

The horizontal dotted line in Fig. 11 shows the Braginskii viscosity of the thermal plasma for $l_{\rm mfp} = 0.2$kpc and $T = 3 \times 10^7$ K, and is larger than $\kappa_{\rm diff}$ in most of the parameter space. Fig. 11 therefore shows that $\Phi < 1$ is plausible in the ICM, and so the CRBI is not completely suppressed by CR diffusion.

7 CONCLUSIONS

In Kempski et al. (2020), we showed that streaming CRs destabilize sound waves in the low-collisionality ICM. The instability arises because the Alfvén speed in low-collisionality plasmas depends on the pressure anisotropy of the thermal gas (equation (10)). This introduces a new unstable form of coupling between CRs and the thermal plasma. In this work, we showed that Alfvénically streaming CRs in a gravitationally stratified medium also destabilize a pressure-balanced mode, more specifically the CR entropy mode. We term this the CRBI because it is the combined action of CR streaming and gravity (buoyancy) that drives the instability. CR entropy modes are highly compressible on small scales (Fig. 3), which drives them unstable in a gravitational field. In the limit of pure CR streaming (no diffusion), there likely is no threshold for the CRBI (see discussion in Sections 4.2 and 5). However, we stress that a global calculation, rather than our local WKB approach, is necessary to check this prediction, especially for parameters that result in slow amplification (Fig. 5). The fastest growth occurs at short wavelengths, where the mode is highly compressible, with growth rates of order $\eta \beta^{1/2} \omega_{\rm ff}$ (equation (53)) where $\eta = p_c/p_g$, $\beta = 8\pi p_g/B^2$, and $\omega_{\rm ff}$ is the free-fall frequency. Our results show that CR streaming in cluster plasmas is a dramatically unstable process and that CR physics is important for understanding wave propagation in the ICM, even for subdominant CR pressures.

We gave a physical overview of the CRBI in Section 3. Instability arises due to gravity acting on the mode's density fluctuations. In standard buoyancy instabilities, such as thermal convection in stars or the MTI (Balbus 2000) and the HBI (Quataert 2008) in clusters, the density fluctuations are due to the background stratification of the plasma. Notably, in the CRBI the density fluctuations at short wavelengths are due to the combined action of CR streaming and pressure balance, independent of the background stratification. We complemented the qualitative physical picture from Section 3 with a quantitative dispersion-relation calculation in Section 4, and showed growth rates and mode properties for a wide range of physical parameters in Figs 3–10.

7.1 Relationship to other instabilities

Previous work on dilute cluster plasmas showed that anisotropic conduction leads to buoyancy instabilities, the MTI and HBI. Fig. 8 shows that these instabilities dominate growth rates at long wavelengths even in the presence of CRs, if the gas scale height is significantly larger than the thermal mean free path, as is the case in cluster cores. The CR-driven instability operates on small scales, precisely where the heat-flux-driven buoyancy instabilities are stable due to magnetic tension. The MTI/HBI and the CRBI of this paper can thus operate simultaneously in cluster plasmas. However, we note that the scale separation between the MTI/HBI and the CRBI is not always so clear: in the more dilute cluster outskirts, where the thermal mean free path is significantly larger, the CRBI can have significant growth rates (of order the free-fall frequency for plausible parameters) even for long-wavelength $kH \sim 1$ modes (Fig. 10).

In Fig. 12, we summarize how the CRBI and the CRAB instability from Kempski et al. (2020) compare to previously identified instabilities that may operate in ICM plasmas. We sketch representative growth rates due to the different instabilities as a function of η. For small η, the HBI/MTI are the fastest growing instabilities operating in the ICM (at large CR pressures we use a dashed line for HBI/MTI because CRs may suppress the HBI, and the CRBI and HBI/MTI can be associated with the same mode; see Fig. 8). For $\eta \gtrsim \beta^{-1/2}$ (recall that $\beta \gg 1$ in the ICM), the growth rate of short-wavelength CR entropy modes driven compressible by CR streaming becomes comparable to or larger than $\omega_{\rm ff}$. For $\eta \gtrsim \beta^{-1/2}$ the CRAB instability of sound waves is also excited (Kempski et al. 2020). The impact of CRs on thermal-instability (TI) growth rates is modest (Kempski & Quataert 2020). The CRAB instability generally drives the fastest growing mode. This, however, does not necessarily mean that for large η the non-linear dynamics are dominated by the CRAB instability, as the saturation of both CR-driven instabilities remains unclear and is the subject of ongoing work. In particular, while the unstable CR entropy modes have smaller growth rates, they also have smaller group speeds and so remain in the region in which they are excited for longer. This is especially true at high β: waves propagating at the Alfvén speed with growth rates of order $\omega_{\rm ff}$ undergo several e-foldings over the distance of one gas scale height (Fig. 5).

7.2 The CRBI and CRAB instability in cluster cores

Heating by streaming CRs may balance cooling in the inner regions of cluster cores (Guo & Oh 2008; Jacob & Pfrommer 2017a, b). For a cooling rate ω_c, this requires CR pressures of order (Kempski & Quataert 2020),

$$\eta \sim \beta^{1/2} \frac{\omega_c}{\omega_{\rm ff}}. \tag{63}$$

The CRAB instability and the CRBI become important for $\eta\beta^{1/2} \gtrsim 1$ and therefore destabilize a CR-heated medium if,

$$\eta\beta^{1/2} \sim \beta \frac{\omega_c}{\omega_{\rm ff}} \gtrsim 1. \tag{64}$$

Observations suggest that $\omega_{\rm ff}/\omega_c \gtrsim 10$ in cluster cores (e.g. McDonald et al. 2010; Hogan et al. 2017). A CR-heated medium is therefore plausibly unstable to the CRAB instability and the CRBI for $\beta \gtrsim 10$, a condition that is likely satisfied in the ICM.

We also note that the CRAB and CR buoyancy instabilities may have, to some extent, similar observational appearances. In particular, although CR entropy modes are pressure-balanced, they are compressible and involve finite gas-pressure fluctuations (balanced by CR-pressure fluctuations). CR entropy modes may therefore masquerade as sound waves if only the thermal-gas fluctuations are measured. Moreover, due to their compressible nature both the CRAB instability and the CRBI may evolve into shock-like structures that resemble the weak shocks observed in the Perseus cluster (Fabian et al. 2003, 2006).

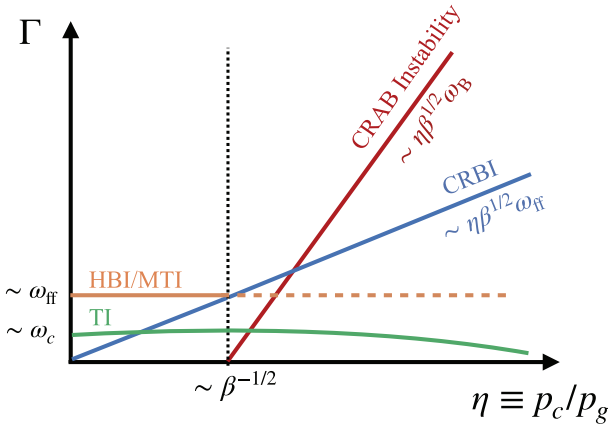

Figure 12. Overview of instabilities in dilute ICM plasmas as a function of $\eta = p_c/p_g$. For small η, the HBI/MTI have the highest growth rates. For $\eta \gtrsim \beta^{-1/2}$, the CRBI has growth rates larger than the HBI/MTI, and the CRAB instability of sound waves is excited. We include approximate growth rates of the CRBI and CRAB instability ($\Gamma \sim \eta\beta^{1/2}\omega_{\rm B}$ for the CRAB instability is valid above the instability threshold and as long as $\Gamma \ll \omega_s$; Kempski et al. 2020). CRs do not significantly affect thermal-instability (TI) growth rates for $\eta \lesssim 1$ (Kempski & Quataert 2020). The CRAB instability drives the fastest growing mode for $\eta \gtrsim \beta^{-1/2}$. However, while the CR entropy modes have smaller growth rates, they also have smaller group speeds and so remain in the region in which they are excited for longer, potentially leading to larger overall amplification.

In the standard picture, AGN in cool cluster cores excite sound waves and IGWs via the time dependence of the AGN jet and the buoyant motion of radio bubbles into the ICM. Kempski et al. (2020) and this work suggest that waves can also be excited by the CR pressure gradient that the bubbles provide. Future simulations will address the non-linear evolution of the CR-driven instabilities. There are two important stages that are crucial for the non-linear evolution and saturation: when the amplitudes become large enough to locally flatten the CR pressure gradient and shut off CR streaming ($\delta p_c/p_c \sim 1/kH$; though this does not necessarily shut off the instability, see Tsung, Oh & Jiang 2022) and when the amplitudes become large enough for the pressure anisotropy to excite kinetic microinstabilities such as the mirror (Barnes 1966; Hasegawa 1969) and firehose (Rosenbluth 1956; Chandrasekhar, Kaufman & Watson 1958; Parker 1958) instabilities (which occur when $|\Delta p| \sim B^2/4\pi$). Upcoming work will address how this additional physics, which is not part of the linear analysis presented here, affects the evolution of the CR-driven instabilities and their impact on the ICM.

7.3 Dependence on CR transport physics

Both the CRBI considered in this work and the CRAB instability in Kempski et al. (2020) are driven by CR streaming at the Alfvén speed. The instabilities therefore operate only if the bulk of CRs in the ICM are self-confined, rather than scattered by an extrinsic turbulent cascade of magnetic fluctuations. According to current theoretical models of MHD turbulence, CR scattering by Alfvénic turbulence is likely negligible, due to the anisotropy of the cascade

(Chandran 2000). The MHD weak cascade of fast modes may be isotropic and more efficient at scattering CRs, and has been proposed as an alternative to self-confinement (Yan & Lazarian 2004). However, because the weak cascade of fast modes is strongly damped in dilute high-β plasmas, and may generally be suppressed by wave steepening (Kadomtsev & Petviashvili 1973; Kempski & Quataert 2022), scattering of energetically important GeV CRs by fast modes is likely suppressed in the high-β ICM. Self-confinement and streaming transport are therefore plausible.

The finite CR mean free path in the frame moving with the self-excited Alfvén waves necessarily implies a correction to the pure Alfvénic streaming model. Significant CR diffusion resulting from this correction can suppress the CRBI (Fig. 7). However, the magnitude and nature of the correction to Alfvénic streaming remains uncertain. In particular, the form of the transport correction turns out to be rather peculiar, as it corresponds to neither streaming nor diffusion (Skilling 1971; Wiener et al. 2013; Kempski & Quataert 2022). We attempted to quantify the magnitude of the *diffusive* part of the transport correction, i.e. the contribution that may suppress the CRBI, in Section 6.4, which was based on the calculation from Appendix B. Fig. 11 shows that the CRBI is usually not suppressed by CR diffusion for expected ICM conditions, although we stress that our calculation of the transport correction is quite uncertain. First-principle simulations of the CR streaming instability, e.g. using particle-in-cell (PIC) or MHD-PIC methods (Holcomb & Spitkovsky 2019; Haggerty, Caprioli & Zweibel 2019; Bai et al. 2019; Bambic, Bai & Ostriker 2021; Bai 2022), are essential for better understanding the physics of streaming-instability-regulated transport and for deriving simplified fluid models like the one used in this paper. Interestingly, so far these simulations tend to produce CR transport speeds that are somewhat larger than predicted analytically using quasi-linear theory (e.g. Bai 2022). It would also be valuable to carry out a more complete version of our calculation—based on CR kinetic theory—to test the conclusions of our simplified fluid treatment (although it is worth noting that existing theories of CR transport are quite uncertain and have difficulties explaining CR measurements in the Milky Way; e.g. Kempski & Quataert 2022, Hopkins et al. 2022).

ACKNOWLEDGEMENTS

We thank Matthew Kunz for useful comments. This research was supported in part by the National Science Foundation under grant number NSF PHY-1748958, by the NSF grant AST-2107872, and a Simons Investigator award from the Simons Foundation. Support for JS was provided by the Rutherford Discovery Fellowship RDF-U001804, which is managed through the Royal Society Te Apārangi.

DATA AVAILABILITY

The calculations from this article will be shared on reasonable request to the corresponding author.

REFERENCES

Amato E., Blasi P., 2018, Adv. Space Res., 62, 2731
Bai X.-N., 2022, ApJ, 928, 112
Bai X.-N., Ostriker E. C., Plotnikov I., Stone J. M., 2019, ApJ, 876, 60
Balbus S. A., 2000, ApJ, 534, 420
Bambic C. J., Bai X.-N., Ostriker E. C., 2021, ApJ, 920, 141
Barnes A., 1966, Phys. Fluids, 9, 1483
Bîrzan L., Rafferty D. A., McNamara B. R., Wise M. W., Nulsen P. E. J., 2004, ApJ, 607, 800
Braginskii S. I., 1965, Rev. Plasma Phys., 1, 205
Breitschwerdt D., McKenzie J. F., Voelk H. J., 1991, A&A, 245, 79
Chandran B. D. G., 2000, Phys. Rev. Lett., 85, 4656
Chandran B. D., Dennis T. J., 2006, ApJ, 642, 140
Chandrasekhar S., Kaufman A. N., Watson K. M., 1958, Proc. R. Soc. Lond. A, 245, 435
Chew C. F., Goldberger M. L., Low F. E., 1956, Proc. R. Soc. Lond. A, 236, 112
Churazov E., Forman W., Jones C., Böhringer H., 2000, A&A, 356, 788
Defouw R. J., 1970, ApJ, 160, 659
Dennis T. J., Chandran B. D. G., 2009, ApJ, 690, 566
Ehlert K., Weinberger R., Pfrommer C., Pakmor R., Springel V., 2018, MNRAS, 481, 2878
Everett J. E., Zweibel E. G., Benjamin R. A., McCammon D., Rocks L., Gallagher John S. I., 2008, ApJ, 674, 258
Fabian A. C., Sanders J. S., Allen S. W., Crawford C. S., Iwasawa K., Johnstone R. M., Schmidt R. W., Taylor G. B., 2003, MNRAS, 344, L43
Fabian A. C., Sanders J. S., Taylor G. B., Allen S. W., Crawford C. S., Johnstone R. M., Iwasawa K., 2006, MNRAS, 366, 417
Farber R., Ruszkowski M., Yang H. Y. K., Zweibel E. G., 2018, ApJ, 856, 112
Farmer A. J., Goldreich P., 2004, ApJ, 604, 671
Field G. B., 1965, ApJ, 142, 531
Guo F., Oh S. P., 2008, MNRAS, 384, 251
Haggerty C., Caprioli D., Zweibel E., 2019, in Proc. 36th International Cosmic Ray Conference (ICRC2019). PoS, Madison, p. 279
Hasegawa A., 1969, Phys. Fluids, 12, 2642
Hlavacek-Larrondo J., Fabian A. C., Edge A. C., Ebeling H., Sanders J. S., Hogan M. T., Taylor G. B., 2012, MNRAS, 421, 1360
Hogan M. T. et al., 2017, ApJ, 851, 66
Holcomb C., Spitkovsky A., 2019, ApJ, 882, 3
Hopkins P. F., Squire J., Butsky I. S., Ji S., 2022, MNRAS, 517, 5413
Hopkins P. F., Squire J., Chan T. K., Quataert E., Ji S., Kereš D., Faucher-Giguère C.-A., 2021, MNRAS, 501, 4184
Jacob S., Pfrommer C., 2017a, MNRAS, 467, 1449
Jacob S., Pfrommer C., 2017b, MNRAS, 467, 1478
Kadomtsev B. B., Petviashvili V. I., 1973, Soviet Phys. Doklady, 18, 115
Kempski P., Quataert E., 2020, MNRAS, 493, 1801
Kempski P., Quataert E., 2022, MNRAS, 514, 657
Kempski P., Quataert E., Squire J., 2020, MNRAS, 493, 5323
Kempski P., Quataert E., Squire J., 2021, MNRAS, 500, 1231
Kulsrud R. M., 2005, Plasma Physics for Astrophysics. Princeton Univ. Press, Princeton
Kulsrud R., Pearce W. P., 1969, ApJ, 156, 445
Kunz M. W., 2011, MNRAS, 417, 602
Lee M. A., Völk H. J., 1973, Ap&SS, 24, 31
Loewenstein M., Zweibel G. E., Begelman C. M., 1991, ApJ, 377, 392
McDonald M., Veilleux S., Rupke D. S. N., Mushotzky R., 2010, ApJ, 721, 1262
Mikhailovskii A., Tsypin V., 1971, Plasma Phys., 13, 785
Nulsen P., Jones C., Forman W., Churazov E., McNamara B., David L., Murray S., 2009, in Heinz S., Wilcots E.eds, AIP Conf. Ser.Vol. 1201, American Institute of Physics, College Park, p. 198,
Parker E. N., 1958, Phys. Rev., 109, 1874
Peterson J. R., Fabian A. C., 2006, Phys. Rep., 427, 1
Quataert E., 2008, ApJ, 673, 758
Quataert E., Jiang Y.-F., Thompson T. A., 2022a, MNRAS, 510, 920
Quataert E., Thompson T. A., Jiang Y.-F., 2022b, MNRAS, 510, 1184
Rafferty D. A., McNamara B. R., Nulsen P. E. J., Wise M. W., 2006, ApJ, 652, 216
Rosenbluth M. N., 1956, Stability of the pinch. Report number LA-2030. Los Alamos Scientific Lab, Los Alamos
Ruszkowski M., Yang H. Y. K., Zweibel E., 2017, ApJ, 834, 208
Schekochihin A. A., Cowley S. C., Rincon F., Rosin M. S., 2010, MNRAS, 405, 291

Sharma P., Chandran B. D. G., Quataert E., Parrish I. J., 2009, ApJ, 699, 348
Skilling J., 1971, ApJ, 170, 265
Snyder P. B., Hammett G. W., Dorland W., 1997, Phys. Plasmas, 4, 3974
Socrates A., Davis S. W., Ramirez-Ruiz E., 2008, ApJ, 687, 202
Squire J., Hopkins P. F., Quataert E., Kempski P., 2021, MNRAS, 502, 2630
Stein R. F., Leibacher J., 1974, ARA&A, 12, 407
Sternberg A., Soker N., 2009, MNRAS, 395, 228
Tsung T. H. N., Oh S. P., Jiang Y.-F., 2022, MNRAS, 513, 4464
Werner N., McNamara B. R., Churazov E., Scannapieco E., 2019, Space Sci. Rev., 215, 5
Wiener J., Oh S. P., Guo F., 2013, MNRAS, 434, 2209
Wiener J., Zweibel E. G., Oh S. P., 2018, MNRAS, 473, 3095
Yan H., Lazarian A., 2004, ApJ, 614, 757
Zhang C., Churazov E., Schekochihin A. A., 2018, MNRAS, 478, 4785
Zhuravleva I. et al., 2016, MNRAS, 458, 2902
Zweibel E. G., 2013, Phys. Plasmas, 20, 055501
Zweibel E. G., 2017, Phys. Plasmas, 24, 055402

APPENDIX A: LANDAU-FLUID CLOSURE FOR LOW-COLLISIONALITY PLASMAS

Here we provide the kinetic MHD equations and the Landau-fluid closure for the heat fluxes used in Section 6.3 and Fig. 10. The kinetic MHD evolution equations for the pressures perpendicular and parallel to the magnetic field are (Chew et al. 1956),

$$\frac{\partial p_\perp}{\partial t} + \nabla\cdot(p_\perp \mathbf{v}) + p_\perp \nabla\cdot\mathbf{v} + \nabla\cdot(q_\perp \hat{\boldsymbol{b}}) + q_\perp \nabla\cdot\hat{\boldsymbol{b}} = p_\perp \hat{\mathbf{b}}\hat{\mathbf{b}} : \nabla\mathbf{v} - \frac{1}{3}\nu_{\rm ii}\Delta p, \tag{A1}$$

$$\frac{\partial p_\parallel}{\partial t} + \nabla\cdot(p_\parallel \mathbf{v}) + \nabla\cdot(q_\parallel \hat{\boldsymbol{b}}) - 2q_\perp \nabla\cdot\hat{\boldsymbol{b}} = -2p_\parallel \hat{\mathbf{b}}\hat{\mathbf{b}} : \nabla\mathbf{v} + \frac{2}{3}\nu_{\rm ii}\Delta p - 3(\gamma-1)\mathbf{v_{st}}\cdot\nabla p_c, \tag{A2}$$

where we made the somewhat uncertain assumption that CR heating is predominantly in the direction parallel to the magnetic field. This is motivated by the fact that CR heating is due to the excitation of parallel-propagating modes, although we note that this is not true if damping by Alfvénic turbulence dominates, which acts to shear the waves to high $k_\perp$. This choice does not, however, significantly affect the results. The above equations are not yet complete, as the heat fluxes are still undetermined. In the Landau-fluid closure, the heat fluxes are set such that the linear behaviour of the fluid model approximately matches the linear response of the fully kinetic thermal plasma (Snyder et al. 1997). The Landau-fluid closure has been popular for modelling collisionless plasmas, as it recovers the fully kinetic linear damping rates (e.g. linear Landau damping of ion acoustic waves) and instabilities (e.g. MRI) of all MHD modes. A convenient form for the heat fluxes, which recovers Braginskii MHD in the collisional limit, is given by (Snyder et al. 1997),

$$q_\perp = -\frac{2c_{s\parallel}^2}{\sqrt{2\pi}|k_\parallel|c_{s\parallel} + \nu_{\rm ii}}\left[\rho\nabla_\parallel\left(\frac{p_\perp}{\rho}\right) - p_\perp\left(1-\frac{p_\perp}{p_\parallel}\right)\frac{\nabla_\parallel B}{B}\right], \tag{A3}$$

$$q_\parallel = -\frac{8c_{s\parallel}^2}{\sqrt{8\pi}|k_\parallel|c_{s\parallel} + (3\pi-8)\nu_{\rm ii}}\rho\nabla_\parallel\left(\frac{p_\parallel}{\rho}\right), \tag{A4}$$

where $c_{s\parallel} = \sqrt{p_\parallel/\rho}$. In Section 6.3 and Fig. 10, we use the linearized versions of (A1)–(A4) instead of the linearized Braginskii MHD equations (31) and (32).

APPENDIX B: CR DIFFUSION COEFFICIENT IN SELF-CONFINEMENT THEORY

In this section, we provide a heuristic calculation of the CR diffusion coefficient in self-confinement theory (a similar calculation can be found in Hopkins et al. 2021). One challenge in this calculation is that leading-order corrections to Alfvénic streaming are often not diffusive. Instead they are better described by a (super-Alfvénic) streaming or sink term (this is the case when linear damping of Alfvén waves dominates; Skilling 1971; Wiener et al. 2013; Kempski & Quataert 2022). For our linear analysis calculation, we are mainly interested in the leading-order *diffusive* correction, which is more likely to suppress the instability than a streaming/sink term.

We calculate the amplitude of waves excited by the CR streaming instability, and the resulting CR scattering frequency, by equating Alfvén-wave growth and damping. We consider a steady state with

$$(\Gamma_{\rm L} + \Gamma_{\rm NL})\frac{\delta B^2}{4\pi} = |\mathbf{v_A}\cdot\nabla p_c|, \tag{B1}$$

where we split the wave damping into a linear and non-linear part ($\propto \delta B^2$). $\Gamma_{\rm L}$ is the sum of all linear damping contributions, turbulent (Farmer & Goldreich 2004), linear-Landau (Wiener et al. 2018), ion-neutral and dust (Squire et al. 2021) damping, although the latter two are likely not important in the hot and dilute ICM. $\Gamma_{\rm NL}$ is the non-linear Landau damping rate (Lee & Völk 1973; Kulsrud 2005), $\Gamma_{\rm NL} = \gamma_{\rm NL}(\delta B/B)^2$, where $\gamma_{\rm NL} \sim k v_{\rm th}$, k is the wavenumber of Alfvén waves resonant with $\sim$ GeV CRs and $v_{\rm th}$ is the ion thermal speed. Equation (B1) becomes a quadratic equation for the wave amplitude

$$\left(\frac{\delta B^2}{B^2}\right)^2 + \frac{\Gamma_{\rm L}}{\gamma_{\rm NL}}\frac{\delta B^2}{B^2} - \frac{\Gamma_{\rm A}}{2\gamma_{\rm NL}}\frac{p_c}{\epsilon_{\rm B}} = 0, \tag{B2}$$

where $\Gamma_{\rm A} \equiv |\mathbf{v_A}\cdot\nabla p_c|/p_c$ is the inverse of the Alfvén crossing time and $\epsilon_{\rm B}$ is the magnetic-field energy density. We first consider the limit $\Gamma_{\rm L} \gg \Gamma_{\rm NL}$. Equation (B2) can then be solved perturbatively to yield

$$\frac{\delta B^2}{B^2} \approx \frac{\Gamma_{\rm A} p_c}{2\Gamma_{\rm L}\epsilon_{\rm B}}\left(1 - \frac{\gamma_{\rm NL}}{\Gamma_{\rm L}}\frac{\Gamma_{\rm A} p_c}{2\Gamma_{\rm L}\epsilon_{\rm B}}\right). \tag{B3}$$

The pitch-angle scattering rate of GeV CRs is $\nu_{\rm CR} \sim \Omega_0 \delta B^2/B^2$, which corresponds to a diffusion coefficient

$$\kappa \sim \frac{c^2}{\nu_{\rm CR}} \approx \kappa_{\rm st} + \kappa_{\rm diff}, \tag{B4}$$

where,

$$\kappa_{\rm st} = \frac{c^2}{\Omega_0}\frac{2\Gamma_{\rm L}\epsilon_{\rm B}}{\Gamma_{\rm A} p_c}, \tag{B5}$$

and

$$\kappa_{\rm diff} = \frac{c^2}{\Omega_0}\frac{\gamma_{\rm NL}}{\Gamma_{\rm L}} \sim \frac{c v_{\rm th}}{\Gamma_{\rm L}}. \tag{B6}$$

$\kappa_{\rm st} \propto |\mathbf{v_A}\cdot\nabla p_c|^{-1}$ reflects the well-known result that for purely linear damping rates the diffusion coefficient is inversely proportional to the CR pressure gradient, so that the diffusion term $\nabla\cdot(\kappa\hat{\boldsymbol{b}}\hat{\boldsymbol{b}}\cdot\nabla p_c)$ ends up not being diffusive at all and is better described as a (super-Alfvénic) streaming or sink term (Skilling 1971; Wiener et al. 2013; Kempski & Quataert 2022). By contrast, $\kappa_{\rm diff}$ is independent of the CR pressure gradient and is therefore a regular diffusion coefficient.

Conversely, if non-linear Landau damping dominates, the CR diffusion coefficient is to leading order (from equation (B2)):

$$\kappa_{\rm NL} \approx \kappa_{\rm diff} \approx \frac{c^2}{\Omega_0}\left(\frac{2\gamma_{\rm NL}\epsilon_{\rm B}}{\Gamma_{\rm A} p_c}\right)^{1/2}. \tag{B7}$$

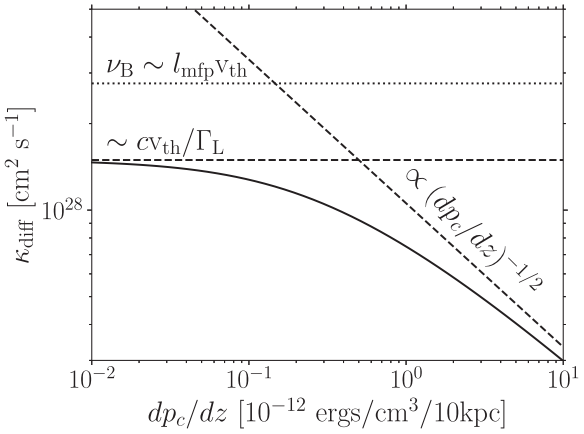

Figure B1. κ_{diff} as a function of the CR pressure gradient for a linear damping rate $\Gamma_L = 10^{-10}\,s^{-1}$, where κ_{diff} is the component of the diffusion coefficient κ that gives rise to actually diffusive behaviour. We estimate κ_{diff} from self-confinement theory by computing the total diffusion coefficient κ from equation (B2) and subtracting κ_{st} (equation (B5)) in order to not include the non-diffusive correction when linear damping dominates. While this method of computing κ_{diff} is not exact, it correctly recovers the diffusive correction in the two asymptotic limits shown by the dashed lines (equations (B6) and (B7)). This suggests that the solid line is a reasonable approximation of the diffusive correction to Alfvénic streaming.

$\kappa_{NL} \propto |\mathbf{v_A} \cdot \nabla p_c|^{-1/2}$ and so we end up with a term that is again not diffusive in the usual sense. However, in linear theory with a background CR pressure gradient, $\nabla\cdot(\kappa \hat{\boldsymbol{b}}\hat{\boldsymbol{b}} \cdot \nabla p_c)$ still gives a term $\propto \kappa k^2$ (where κ depends on the background gradient) and is therefore linearly diffusive.

In the high-β ICM, linear Landau damping (Wiener et al. 2018) is likely the most important linear damping rate. For turbulence injected on ∼10 kpc (common scale of the radio bubbles) with perturbations comparable to the Alfvén speed, the damping rate of $k \sim r_L^{-1}$ Alfvén waves excited by GeV CRs (where r_L is the GeV CR gyroradius) is

$$\Gamma_L \sim \frac{0.4 v_{th}}{(r_L L_{turb})^{1/2}} \sim 10^{-10}\,s^{-1} \frac{v_{th}}{10^8 cm\ s^{-1}} \left(\frac{L_{turb}}{10\ kpc}\right)^{-1/2} \left(\frac{B}{1\ \mu G}\right)^{1/2}. \quad (B8)$$

We plot κ_{diff}, i.e. the component of the diffusion coefficient κ that gives rise to actually diffusive behaviour, as a function of the CR pressure gradient in Fig. B1 (see also Fig. 11 for a different version of this plot). We calculate κ_{diff} by computing the total diffusion coefficient κ from equation (B2) and subtracting κ_{st} (equation (B5)) in order to not include the non-diffusive correction when linear damping dominates. Simply subtracting κ_{st} to obtain the diffusive correction is not exact. However, it correctly recovers the two asymptotic limits (equations (B6) and (B7) and the dashed lines in Fig. B1). This suggests that the solid line in Fig. B1 is a reasonable approximation of the diffusive correction to Alfvénic streaming.

For large CR pressure gradients, the streaming instability reaches large amplitudes (for a fixed linear damping rate) and non-linear Landau damping is more important than linear damping mechanisms. The resulting diffusion coefficients are $\propto (dp_c/dz)^{-1/2}$. For small CR pressure gradients, linear damping dominates as the amplitudes reached by the streaming instability are not large enough for non-linear Landau damping to be important. The diffusion coefficient is constant and approximately given by equation (B6). The horizontal dotted line in Fig. B1 is the anisotropic viscosity of the thermal gas for $l_{mfp} \sim 0.2$ kpc and $T = 3 \times 10^7$ K. It is therefore plausible to expect $\Phi < 1$ in cluster cores and the CRBI remains active, though is likely partially suppressed (Fig. 7).

This paper has been typeset from a TEX/LATEX file prepared by the author.